coatings

MDPI

Review

Progress in Microstructure Design and Control of High-Hardness Fe-Based Alloy Coatings via Laser Cladding

Lipei Liu [1], Yinghua Lin [1,*], Longsheng Peng [2,3], Xin Kang [4,*] and Xinlin Wang [1]

[1] Hunan Province Key Laboratory for Ultra-Fast Micro/Nano Technology and Advanced Laser Manufacture, College of Mechanical Engineering, University of South China, Hengyang 421001, China; lipeiliu97@163.com (L.L.); wxl_ly000@aliyun.com (X.W.)
[2] Hunan Lifang Roller Co., Ltd., Hengyang 421681, China; flslfls@163.com
[3] Hunan Advanced Manufacturing Engineering Technology Research Center for High Wear-Resistant Alloy Materials, Hengyang 421681, China
[4] School of Mechanical, Electrical and Information Engineering, Putian University, Putian 351100, China
* Correspondence: lyh351258@163.com (Y.L.); tokangxin@163.com (X.K.)

Abstract: High-hardness iron-based alloy coatings are extensively utilized in aerospace, automotive, and industrial equipment due to their exceptional wear resistance and long service life. Laser cladding has emerged as one of the primary techniques for fabricating these coatings, owing to its rapid cooling and dense microstructure characteristics. However, the production of high-hardness iron-based alloy coatings via laser cladding continues to face numerous challenges, particularly when controlling the morphology, quantity, and distribution of the reinforcing phases, which can lead to cracking during processing and service, thus compromising their usability. The cracks of the cladding layer will be suppressed through good microstructure design and control, resulting in a wide range of performance for high-hardness Fe-based alloy coatings. This paper reviews recent advancements in the design and control of the organization and structure of high-hardness iron-based alloy coatings from the perspectives of material composition, processing parameters, and external assistance techniques. It summarizes the properties and applications of various materials, including different alloying elements, ceramic particles, and rare earth oxides, while systematically discussing how processing parameters influence microstructure and performance. Additionally, the mechanisms by which external auxiliary energy fields affect the melt pool and solidified microstructure during laser cladding are elucidated. Finally, the future development directions of laser cladding technology for high-hardness iron-based coatings are anticipated, emphasizing the need for further quantification of the optimal coupling relationships among the gain effects of composite energy fields.

Keywords: laser cladding; surface strengthening; Fe-based alloy; high hardness; microstructure design and control

Citation: Liu, L.; Lin, Y.; Peng, L.; Kang, X.; Wang, X. Progress in Microstructure Design and Control of High-Hardness Fe-Based Alloy Coatings via Laser Cladding. *Coatings* **2024**, *14*, 1351. https://doi.org/10.3390/coatings14111351

Academic Editor: Avik Samanta

Received: 28 September 2024
Revised: 21 October 2024
Accepted: 22 October 2024
Published: 24 October 2024

1. Introduction

As critical equipment components face increasingly stringent operating conditions and as materials science continues to evolve [1,2], there is a heightened demand for the development and application of high-hardness coatings [3]. Compared to traditional methods such as plasma welding and thermal spraying, laser cladding offers significant advantages in producing high-hardness coatings. This is due to its rapid cooling rate, high deposition efficiency, and capability to produce fine and dense microstructures in the formed component [4–6]. However, the rapid heating and cooling characteristics inherent in laser cladding [7,8], along with the differences in melting point and thermal conductivity of the coating materials [9,10], can result in high temperature gradients during the coating formation process, leading to elevated residual stresses, stress accumulation, and solidification segregation. These factors collectively increase the susceptibility to cracking. Particularly when preparing high-hardness coatings using laser cladding, the

balance—or competing relationship [11]—between strength and toughness can further intensify the cracking phenomena. Such cracking issues pose significant challenges to the broad adoption of these coatings in industrial settings.

Compared to Co-based [12] and Ni-based [13] alloys, the primary advantage of Fe-based alloys is their widespread availability and affordability [14]. Furthermore, as the matrix materials for many engineering components in contemporary applications are primarily steel-based structural materials, utilizing iron-based cladding materials ensures excellent wetting properties, resulting in a robust bond with the substrate [15–17]. However, laser cladding with iron-based alloy powder has certain limitations. These include poor self-fusibility, reduced oxidation resistance, and susceptibility to porosity and inclusions [18–20]. Moreover, high-hardness iron-based coatings often have a higher concentration of brittle phases, such as borides and carbides [19], which can induce cracking during the rapid thermal cycling inherent in the cladding process. These phenomena can cause coating failures and render the coating's microstructure inadequate for the stringent requirements posed by high-load friction and wear components [21]. The precise structural design and regulation of laser-cladded high-hardness iron-based alloy coatings are necessary to suppress the initiation and propagation of intergranular cracks during their manufacturing and operational phases, thereby enhancing the surface properties of coatings, including wear resistance, corrosion resistance, and high-temperature oxidation resistance. Advancing these methods is crucial for promoting the application of high-hardness iron-based alloy laser cladding.

Concerning the microstructural design and regulation of high-hardness Fe-based alloy coatings, this study first delves into the impact of the coating material's composition (alloy elements, ceramic particles, and rare earth oxides) on the microstructure and attributes of the coatings. Next, it highlights the regulatory influences of laser process parameters (such as laser power, scanning speed, and powder feeding rate) and auxiliary treatment processes on the solidification microstructure and coating properties. Finally, challenges encountered in the preparation of laser-cladded high-hardness Fe-based alloy coatings are detailed and examined, and prospective research directions are outlined.

2. Composition of Coating Materials

The performance of the cladding layer is predominantly determined by the cladding material [22]. Therefore, a logical and scientific design of the cladding powder formula emerges as a vital aspect of experimental research. Beyond aligning with requirements such as similarity in melting points, superior wettability, and comparable thermal expansion coefficients, the design of cladding materials should also leverage their inherent performance advantages. An appropriate composition design of the powder material is pivotal for achieving high-quality alloy coatings. Considering these aspects, we present a review of the current research endeavors focused on enhancing the performance of Fe-based alloy coatings. This enhancement is achieved by modifying alloy elements, incorporating ceramic particles, and adjusting the composition ratios of cladding materials with the addition of rare earth oxides.

2.1. Alloy Element Design

Owing to the distinct atomic sizes, chemical properties, and structural characteristics of various elements, their ability to impede dislocation motion directly contributes to the alloy's high strength. Techniques such as altering the lattice structure of the matrix to facilitate grain refinement and increasing the quenching capacity of the matrix can indirectly enhance the alloy's strength. Broadly, different alloy elements exert varied influences on their resulting microstructures and their comprehensive properties [23]. It becomes essential, then, to account for the impacts of these diverse elements on the microstructure and properties and to judiciously select alloy elements in line with laser cladding specifics. Therefore, an in-depth comprehension of the mechanisms behind the influences of these

alloy elements is instrumental in the development of high-performance alloy coatings. Table 1 summarizes the mechanisms of action for common alloying elements.

Table 1. Mechanisms of common elements.

Element	Mechanism
B	The addition of this element can enhance carbon activity and promote the formation of carbides [24,25].
Si	The addition of this element can enhance both dislocation strengthening and solid solution strengthening [26].
Mo	The addition of this element can increase the lattice distortion, easily refine the alloy structure, and improve the hardness and other properties [27].
Nb	The addition of this element can increase the lattice distortion and the high-hardness Laves phase which is easy to precipitate, thus improving the hardness of the coating [28].
V	The addition of this element can enhance grain refinement strengthening and improve the corrosion resistance of the coating [29].
Mn	The addition of this element can enhance austenite stability and reduce the permeability of the coating [30].
Cr	The addition of this element can enhance both grain refinement strengthening and solid solution strengthening [31].

B elements exhibit a lower diffusion rate within hard phase structures and possess a reduced solubility in the metallic matrix. The enrichment of B elements can influence phase transformations and decrease the energy required for phase formation. The types of eutectic carbides in conventional high-strength iron-based coatings are primarily M_2C, MC, and M_6C, which are characterized by their limited ductility. On the other hand, M_3C demonstrates superior fracture toughness. Lentz et al. [24,25] found that introducing an appropriate quantity of B elements can promote the precipitation of the Fe_3C eutectic structure within iron-based composite materials. B elements can also enhance the carbon activity in the liquid phase, enabling the easier precipitation of Fe_3C eutectic structures even in regions with diminished carbon content. Feng et al. [32] incorporated trace amounts of B while fabricating a 42CrMo iron-based coating. As illustrated in Figure 1, with a progressive increase in the B content of the coating, the reinforcing phase transformed from NbC-type carbides to $Cr_{23}C_6$-type carbides, ultimately transitioning into Fe_3C-type carbides. Integrating B proves beneficial in lowering the formation energy of Fe_3C. Upon reaching a B content of 0.75%, a eutectic microstructure composed of Fe_3C-type carbides and γ-Fe is formed, with a hardness exceeding 900 $HV_{0.5}$. (The value 0.5 indicates the Vickers hardness measured under a load of 500 g, while 0.1, 0.12, 0.2, 0.3, and 1 in the following text represent the Vickers hardness measured under loads of 100 g, 120 g, 200 g, 300 g, and 1000 g, respectively). Under this condition, the coating exhibits peak compressive strength and ductility.

The incorporation of Si elements is pivotal in laser cladding. It effectively inhibits grain growth and facilitates grain refinement. Wang et al. [33] investigated the impact of Si content on the microstructure and performance of FeCoNiBSiNb laser-cladded coatings. An optimal amount of Si suppresses the formation and growth of dendritic structures, yielding a more homogeneous coating microstructure. The coating's average hardness surged from 719 $HV_{0.1}$ (without Si) to 930 $HV_{0.1}$, paired with an increase of approximately 700 MPa in fracture strength. In another study, Liang et al. [34] integrated single-crystal silicon powder in varying mass fractions to enhance the quality of Fe60 alloy coatings. Their findings suggested that an appropriate Si content improved the bonding efficacy between the substrate and the coating while also enhancing the microstructural homogeneity. At a mass ratio of 20:1, the coating hardness peaked at 66 HRC. Additionally, Dong et al. [26] observed that in 316 L stainless steel coatings, the introduced Si elements accumulated as nano-sized

silicon dioxide particles at the cellular substructure's grain boundaries. Under the influence of thermal stresses during solidification, these nano silicon dioxide particles induced the formation of dense dislocation structures around them. Such dislocation structures disrupted the growth of columnar solidification structures, enhancing the formation of cellular structures. This process improves the coating's performance and microstructure.

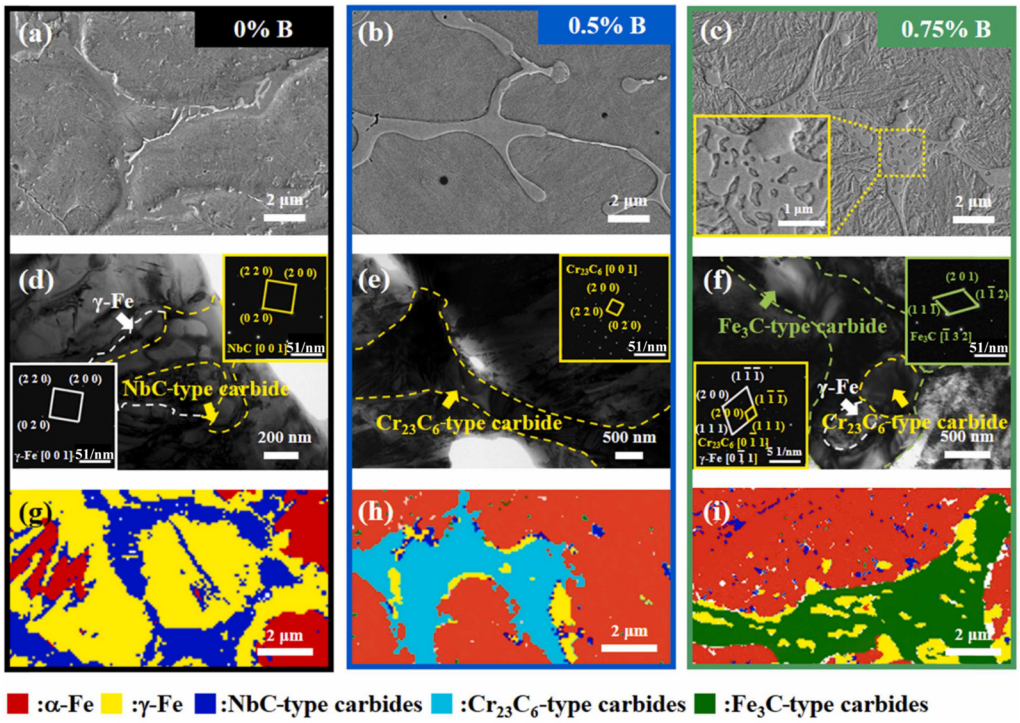

Figure 1. Carbides present in 0% B, 0.5% B, and 0.75% B coatings: (**a**–**c**) scanning electron microscopy images of carbides; (**d**–**f**) transmission electron microscopy images of eutectic structure and corresponding selected area electron diffraction of carbides; and (**g**–**i**) phase image of carbides [32].

Mo is a vital alloying element in steel and cast iron, renowned for its pronounced hardenability and solid-solution-strengthening effects. Li et al. [27] found that incorporating Mo into Fe901 alloy coatings refines the grain structure and promotes the formation of hard phase Mo_2FeB_2. Mo tends to aggregate near grain boundaries, facilitating both grain refinement and solid solution strengthening. The average hardness of the coating with 4.8 wt% Mo content reached 720.2 $HV_{0.2}$, approximately 3.6 times that of the substrate. In a separate study, Chen et al. [35] prepared Fe-Mo coatings with varying Mo content on 65 Mn steel plowshares. Introducing Mo caused the precipitation of brittle phases, such as the σ phase, distributed along grain boundaries, resulting in a minor decline in coating impact toughness. However, as the Mo content increased, dendritic growth was promoted, leading to finer grain sizes. Consequently, the coating hardness peaked at 894 $HV_{0.12}$, nearly double that of the matrix. Cao et al. [36] investigated the influence of Mo content on the microstructure and properties of Fe-Cr-Ni-B-Si composite coatings. An optimal Mo content transformed the Fe-based composite coatings' microstructure from coarse columnar grains into a disordered amorphous matrix, accompanied by the generation of nano-precipitates. This transformation significantly increased the coatings' microhardness to 1100 $HV_{0.5}$ and improved their resistance to plastic deformation. Ma et al. [37] performed laser cladding of iron-based coatings with varying Mo content on Q235 steel surfaces. With increasing Mo content, the coating's structure progressively refined. The content of high-hardness $M_{23}(C, B)_6$-type boron carbides in the eutectic structure increased while the formation of the softer $M_7(C, B)_3$-type boron carbides diminished. This wear resistance improvement resulted in coating microhardness levels consistently exceeding 700 $HV_{0.5}$, with only minor variations.

Compared to other elements, Nb possesses a notably large atomic radius, low solubility with other elements during solidification, and a propensity to cluster at the solid–liquid interface, inhibiting grain growth. Wang et al. [38] fabricated Fe-Cr-Mo-Co-C-B-Nb alloy coatings on 45 steel surfaces with Nb mass fractions of 0%, 2%, 4%, and 6%. As demonstrated in Figure 2, the crystalline zone at the interface between the substrate and the coating diminishes with increasing Nb content. From the enlarged view of A in Figure 2a, it can be seen that there are many pores in the bonding zones without Nb addition. The inclusion of Nb results in the disappearance of pores in the bonding zone, leading to a more cohesive interface and improved bonding strength. Additionally, introducing a modest amount of Nb to both low-carbon steel and stainless steel not only causes significant lattice distortion but also promotes the formation of fine secondary phases, substantially enhancing the mechanical attributes of the cladding layer. In a separate study, Liu et al. [28] infused varying Nb concentrations into 316 L stainless steel cladding coatings. As the Nb content increased, lattice distortion occurred, bolstering the solid solution effect, refining the grain size, and augmenting the formation of new Laves phases. These factors enhanced the coating's hardness. Moreover, with the integration of Nb, it accumulates on the surface, forming an oxidized Nb film. Coatings containing a 1% Nb mass fraction demonstrated superior corrosion resistance. However, an excessive Nb presence increased susceptibility to corrosion, consequently compromising the coating's corrosion resistance.

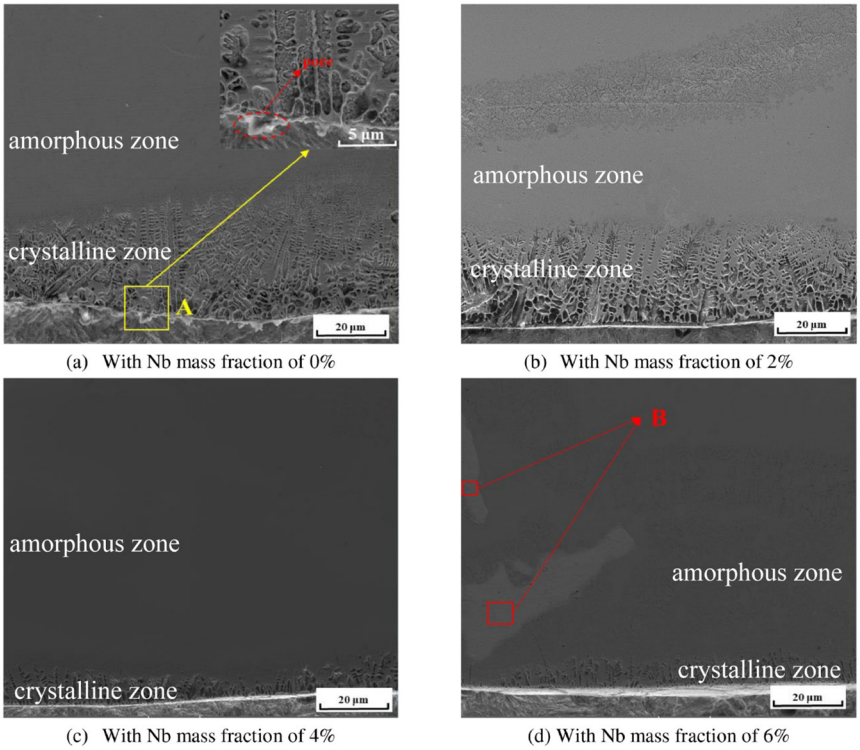

Figure 2. Microstructure of the coatings with different Nb mass fractions [38]. ("A" refers to the yellow boxed area in (**a**), with an enlarged view of "A" in the upper right corner. "B" refers to the white area in (**d**), while the white area is rich in Nb and Mo elements.).

In iron-based alloys, constituent elements vary in atomic size, chemical properties, and structural characteristics. The interactions among these elements result in the formation of diverse alloy phases. The attributes, structure, and concentration of these phases directly influence the alloy's performance. Addressing the need for laser cladding re-manufacturing of corrosion-resistant and wear-resistant critical components, Shan et al. [39] utilized a "material genetics" design approach based on classical phase theory for iron-based alloys. They established a material gene design database system, emphasizing key gene designs pertinent to corrosion and wear. Their optimization yielded a novel 50Cr12Ni3Mo2W6Co5BiTi3CeO_2

iron-based alloy composition. In contrast to the 50Cr6Ni2Y alloy prepared using traditional composition design methods, this new iron-based alloy coating exhibited enhanced resistance to corrosion and wear. Yao et al. [40] employed a supersaturated solid solution alloy design to fabricate Fe-C-Cr-Ni-Mo-W-V-Ti-Ce powder. The resultant coating featured martensite, residual austenite, and in situ-generated reinforcing particles devoid of surface cracks. Achieving a hardness of 65 HRC, its hardness, wear resistance, and toughness surpassed that of the substrate. In real-world applications, the interplays between alloy composition, microstructure, and performance are intricate. Contemporary research often focuses on the impact of individual element contents on coating performance. It is crucial to delve deeper into understanding the interaction mechanisms among the constituent elements and to consider both microstructure and performance from the outset of material development.

2.2. Adding Ceramic Particles

Beyond incorporating specific elements for second-phase strengthening, introducing ceramic particles into iron-based alloys is another method to form reinforcing phases, which enhances the wear resistance of the coatings. This is accomplished using either the "direct addition" or the "in situ synthesis" method. By merging the high ductility and toughness of metallic materials with the exceptional qualities of ceramics—such as high hardness, wear resistance, and corrosion resistance—a synergistic effect emerges, considerably improving the service performance of components. Table 2 provides a detailed comparison of the addition methods, hard particles, and the resulting mechanical properties of iron-based alloy coatings reinforced with ceramic particles.

Table 2. Ceramic particle-reinforced iron-based coating.

Addition Method	Hard Particles	Phase Composition	Hardness	Mechanical Properties	Ref.
Directly added	WC	FCC, WC, M_6C	874 $HV_{0.2}$	No cracks; microhardness increased by 4.2 times; significant wear resistance improvement	[41]
Directly added	WC-14Co	α-Fe, γ-Fe, WC, MoC, $M_{23}C_6$	937.6 $HV_{0.1}$	No cracks; significantly improved microhardness; reduced wear amount	[42]
Directly added	WC	γ austenite, ε martensite, Fe_6W_6C	650 $HV_{0.2}$	No cracks; microhardness increased by over 2 times; friction coefficient reduced by 1/4	[43]
In situ synthesis	WC	α-Fe, $(Cr, W)_{23}C_6$, WC	827 $HV_{0.5}$	Hardness increased by 1.43 times; significant friction coefficient decrease	[44]
In situ synthesis	TiC	Fe, $FeTiO_3$, TiC	950 $HV_{0.1}$	No cracks; hardness was 3 times higher than matrix	[45]
In situ synthesis	TiC	Ferrite, Fe_3C, TiC, TiCx, FeTi, Fe_2Ti	1022 $HV_{0.2}$	Microhardness and wear resistance increased with the increase in TiC or TiCx content	[46]
Directly added	Cr_3C_2 + MoS_2	Fe-Cr-Ni, $(Cr, Fe)_{23}C_6$, MoS_2, CrS	746 $HV_{0.2}$	Significantly improved wear resistance	[47]
Directly added	NiCr-Cr_3C_2	Martensite, Cr_3C_2, Cr_7C_3, $(Cr{\cdot}Fe)_7C_3$	1100 $HV_{0.2}$	Higher thermal fatigue resistance and wear resistance than matrix	[48]
In situ synthesis	NbC	NbC, Fe_2B, B_4C, solid solution	866 $HV_{0.5}$	Significantly improved hardness; abrasive wear shifted to adhesive wear	[49]
In situ synthesis	VC	α-Fe, VC, M_7C_3, $M_{23}C_6$ (M: Cr and Fe)	850 $HV_{0.2}$	Uniform microhardness distribution; significantly improved hardness and wear resistance	[50]
In situ synthesis	Al_2O_3	γ-Fe, Fe_3C, $(Cr, Fe)_7C_3$, Al_2O_3	725 $HV_{0.1}$	Significantly increased microhardness of coating and heat-affected zone	[51]

2.2.1. Direct Addition of Ceramic Particles

The direct addition approach entails the mechanical mixing of ceramic particles with metal powder. Due to ceramics' high melting point, only a small portion of these particles melt during the laser cladding process. The remaining unmelted ceramic particles function as reinforcing phases, providing strengthening effects [52,53].

When ceramic particles are added in insufficient quantities, they fail to provide adequate reinforcement. On the other hand, excessive addition leads to significant disparities in physical properties, such as thermal expansion coefficients, melting points, and wetting behavior, between the composite material and the matrix. These disparities can lead to increased thermal stresses and a rise in the content of eutectic phases as the volume fraction of ceramic particles increases. Furthermore, the distribution of these eutectic phases becomes more uneven, resulting in a more brittle coating with a higher susceptibility to cracking [54,55]. Thus, to effectively enhance service performance, it is crucial to control the mass fraction of the added ceramic particles to produce high-quality coatings free of cracks or voids. Lu et al. [56] examined the impact of varying WC content on the microstructural characteristics and wear performance of Fe104 alloy coatings. The W and C elements diffused into the iron matrix, and as WC content increased, a portion of Fe_3W_3C transitioned into the more stable and harder Fe_6W_6C phase. This led to an improved microhardness and wear resistance of the coating. Zhu and colleagues [57] employed laser cladding technology to produce 410 martensitic stainless steel coatings with different TiC ceramic particle concentrations. The inclusion of TiC ceramic particles notably refined the lamellar martensite. When the content reached 10 wt%, the coating's hardness surged to 634 $HV_{0.2}$, a significant increase compared to the 462 $HV_{0.2}$ hardness of the TiC-free coating. However, laser-cladded coatings with a high 15 wt% TiC content exhibited microcracks and pores.

The size of ceramic particles can influence their solubility, thereby affecting the microstructure and properties of the coatings. Li et al. [58] found that small-sized WC had a positive effect on the uniform refinement of the organization of Fe-based composite coatings, while the opposite was true for large-sized WC. Utilizing laser cladding technology, Qi et al. [59] developed Fe-WC composite coatings and noted that the combustion loss rate of WC particles was inversely proportional to the average particle size of localized WC particles. Zou et al. [60] generated WC powder via plasma rotating electrode atomization and found that smaller WC particles facilitated enhanced wear resistance.

2.2.2. In Situ Synthesis of Ceramic Particles

The direct addition method offers a wide range of material choices, a straightforward preparation process, and controllable particle sizes. However, it is susceptible to poor interface bonding due to differences in thermal material properties, as well as issues related to the burning of ceramic phases. These issues can lead to coating cracking or delamination, which can significantly reduce the coating's lifespan [61]. In 1976, Soviet scholars introduced the concept of in situ composite materials, where different elements or compounds undergo chemical reactions under specific conditions, producing one or more ceramic phase particles within the metal matrix [62]. Compared to the direct addition method, in situ synthesis mitigates concerns related to surface contamination between the matrix material and ceramic particles. Moreover, in situ-synthesized ceramic reinforcing phases are uniformly dispersed and distributed within the matrix, ensuring optimal wetting and interface bonding properties with the matrix [63,64]. Chen et al. [49] used a mixture of Nb and boron carbide powder to produce in situ NbC-reinforced iron-based coatings on medium carbon steel surfaces. Figure 3 illustrates the principle of in situ laser cladding for generating NbC ceramic particles. The composite coatings primarily consist of reinforcing phases (NbC, Fe_2B, and B_4C) and the matrix (solid solution). In situ-formed NbC particles at grain boundaries enable dispersion and fine-crystal strengthening effects. Ren et al. [65] employed ultra-high-speed laser cladding technology to fabricate defect-free in situ VC-reinforced X-M6V coatings. In situ synthesis allows the coating to avoid stress concentration caused by the aggregation of reinforcing phases, ensuring a more uniform

particle distribution. The extremely high cooling rate, combined with uniform VC precipitation, contributes to both fine-crystal strengthening and second-phase strengthening, thus enhancing the coating's hardness and wear resistance. The coating's low wear loss and reduced surface roughness indicate its suitability for use with minimal or no subsequent finishing. This synergistic approach of ultra-high-speed laser cladding and in situ synthesis holds potential for broader applications in ceramic-reinforced composite coatings.

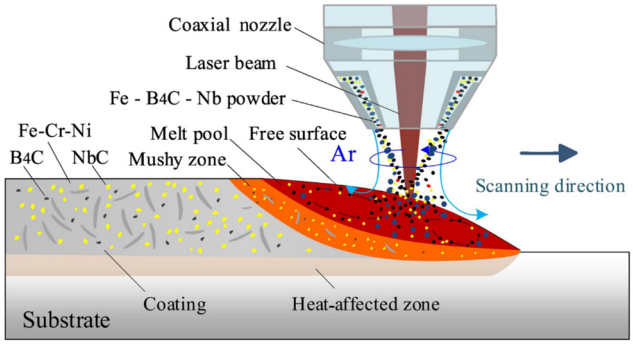

Figure 3. Principle of in situ ceramic particle synthesis via laser cladding [49].

Due to the poor wetting between ceramics and the metal matrix, the bonding interface between the ceramic and metal matrix can become a potential source of cracks under alternating stresses. This issue significantly diminishes the wear resistance and corrosion resistance of single ceramic-reinforced coatings. In composite ceramics, ceramic particles interact with each other, effectively preventing the detachment of ceramic particles from the coating matrix [66]. This has made them an emerging focus in industrial applications. Zhu et al. [67] successfully fabricated an Al_2O_3/TiC composite ceramic coating on a 16Mn steel substrate using Fe60 alloy powder and Ti_3SiC_2 particles. They observed that the TiC carbides of Al_2O_3/TiC composite ceramics have a dragging effect on the Al_2O_3 precipitates and prevent the reinforcements from being ripped out from the matrix.

2.3. Addition of Rare Earth Oxides

Rare earth elements, often termed "industrial gold", are prized for their unique electron structure and highly reactive chemical properties. In metallurgy, they are frequently utilized as spheroidizing and nucleating agents to enhance casting quality. Upon interaction with oxygen and sulfur, rare earth elements readily form high-melting-point oxides and sulfides, thereby facilitating the deoxidation, desulfurization, and morphological transformation of inclusions. Appropriately introducing rare earth elements into laser cladding powders can effectively control the coating's microstructure, improve its morphology, and enhance its surface properties [68,69].

During the cooling process of coatings, rare earth oxides can serve as crystallization nuclei, increasing nucleation rates. They tend to accumulate near grain boundaries, obstructing grain growth and thereby improving the coating's hardness and wear resistance [70]. Jiang et al. [71] added Y_2O_3 when preparing FeCrAlTiC coatings and found that Y_2O_3 reacted with TiC near the grain boundaries to form two oxides, $Y_2Ti_2O_7$ and Y_2TiO_5, which changed the morphology of TiC from short rod-like to spherical, resulting in a decrease in the wetting ratio at the grain boundaries. Compared to the coatings without Y_2O_3, the microhardness of the coatings increased by 9.88%. Wang et al. [72] aimed to prevent the formation of coarse columnar grains during the cladding process by introducing varying quantities of La_2O_3 into the coating, as depicted in Figure 4. Coatings containing 1 wt% La_2O_3 displayed no significant columnar grains. However, in 2 wt% La_2O_3 coatings, a minimal presence of columnar crystals was noted. Compared to La_2O_3-free coatings, the columnar crystals in the 2 wt% La_2O_3 coating were confined mainly to the interface, and both their size and quantity were reduced.

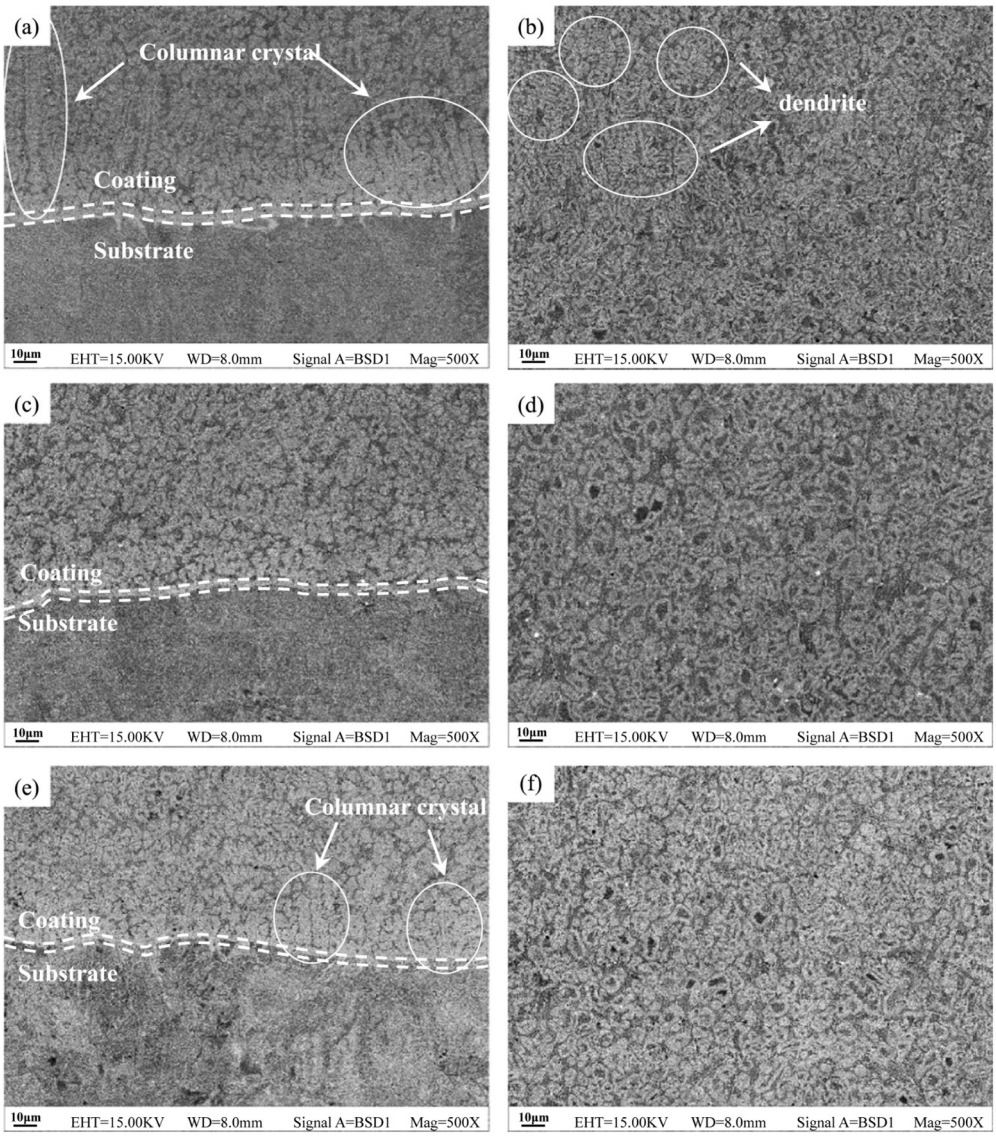

Figure 4. Microstructure of the interfacial binding region and the middle part of the coating: (**a**,**b**) 0 wt% La_2O_3; (**c**,**d**) 1 wt% La_2O_3; and (**e**,**f**) 2 wt% La_2O_3 [72].

An appropriate addition of rare earth elements can enhance the coating's microstructure, modify the morphology of ceramic phase particles, and ensure their uniform distribution in the cladding layer. Cai et al. [73] used laser cladding to prepare TiC/Fe-based composite coatings with CeO_2 on the surface of $Cr_{12}MoV$ steel. The research revealed that in the absence of rare earth elements, the TiC ceramic particles exhibited irregular shapes, significant size variations, and a degree of agglomeration. An appropriate addition of rare earth elements effectively promoted the spheroidization and refinement of ceramic particles, ensuring a homogeneous distribution. However, adding excessive rare earth elements can cause ceramic particle burning loss, inhibit the formation of secondary precipitates, and result in particle agglomeration. Chen et al. [74] assessed the impact of adding varying amounts of CeO_2 on the microstructure and performance of laser-cladded ceramic-reinforced $Fe_{78.5}Cr_{15.6}Ni_{4.0}Si_{0.7}$ coatings. They identified that when the CeO_2 content exceeded 3%, no TiC particles precipitated within the coating. An excess of rare earth elements suppressed the secondary precipitation of TiC ceramic particles after the initial TiC ceramic particles decomposed into Ti and C elements.

Rare earth elements have a high affinity for oxygen, preventing the oxidation of other reactive alloying elements. This attribute significantly enhances the coatings' resistance to high-temperature oxidation and corrosion. Zhang et al. [75] examined the high-temperature oxidation resistance of iron-based composite coatings containing the rare earth oxide Y_2O_3 at 600 °C. Y_2O_3 aggregates at grain boundaries, reducing the diffusion of metal ions towards grain boundaries. This considerably diminishes the corrosion rate associated with gas-phase oxidation and inhibits the surface oxidation of the cladding layer.

3. Laser Cladding Process Parameters

Beyond the primary consideration of cladding material, adjusting laser process parameters can directly influence the coating's microstructure and its formative quality. These process parameters are intricately connected to the coating's structural properties; modifying them reflects changes in the interactions among the laser, powder, and substrate [18]. Variations in these parameters can impact the heat accumulation during the cladding process [76], cooling rates of the molten pool [77], thermal cycling pattern [78], and Marangoni flow behavior [79]. Consequently, these changes can affect the coating's microstructure, performance, and surface quality. Among these, laser power, scanning speed, and powder feed rate have the more significant impact on coating quality [80].

3.1. Laser Power

Laser power is one of the most critical parameters in laser cladding, directly influencing the microstructure and properties of the clad layer. Excessive laser power can cause the over-sintering of the powder, exacerbating deformation and cracking in the cladding layer. Conversely, insufficient laser power can result in the incomplete melting of the powder material, leading to issues such as voids and balling. Within a certain range, adjusting the laser power and changing the power density can regulate the cladding layer's depth, promoting dynamic solidification and reducing defects such as cracks and pores. Mao et al. [81] analyzed the differences in the microstructure and microhardness of iron-based alloy coatings at two laser power levels: 2.5 kW and 2.8 kW. They observed that, within a specific power range, as the laser power increased, the melt pool absorbed more heat. This extended the solidification time, enhanced substrate melting, increased dilution, expanded dendrite size, and promoted directional solidification. As a result, the hardness of the coatings decreased from 864–984 $HV_{0.3}$ to 660–851 $HV_{0.3}$. Xie et al. [82] prepared Fe314 alloy cladding layers on an EA4T steel substrate using various laser powers (1.5 kW, 1.8 kW, 2.1 kW, and 2.4 kW). As shown in Figure 5, with an increase in laser power, the melt pool absorbed more heat. This prolonged the time the melt pool remained at a high-temperature state, allowing more time for grain growth. This led to the formation of larger columnar grains and diminished the effect of fine-grain strengthening. Consequently, the coating's microhardness decreased with increasing laser power.

3.2. Scanning Speed

Scanning speed has a similar impact to that of laser power. When other process parameters are kept constant, an exceedingly low laser scanning speed prolongs the interaction time between the laser beam and the cladding powder. This elevates the coating temperature and intensifies substrate melting and dilution, resulting in a decline in the surface quality and wear resistance of the cladding layer. On the other hand, an excessively high scanning speed reduces the interaction time between the laser beam and the cladding powder, diminishing dilution and impairing the metallurgical bonding between the coating and the substrate, thereby reducing wear resistance. Jiao et al. [83] deposited a layer of T15M high-speed steel alloy powder onto a Q235 substrate at different scanning speeds (100 mm/min, 200 mm/min, and 300 mm/min). Among the three, the coating produced at a scanning speed of 200 mm/min exhibited the smallest grain size, highest solid solubility, and most substantial average hardness, reaching 1050 $HV_{0.1}$. However, as the scanning speed escalated to 300 mm/min, the wear performance of the coating deteriorated, with

a notable amount of material peeling off. Li et al. [84] utilized high-speed laser cladding technology to deposit an Fe-Co-B-Si-Nb amorphous coating on the surface of 45 medium carbon steel at varying scanning speeds. A large volume fraction of amorphous phases and some dendrites was contained within the coating. The distances between secondary dendrite arms and cooling rates in different areas of the high-speed laser-cladded samples under varying scanning speeds are illustrated in Figure 6. As the scanning speed increased, the distance between secondary dendrite arms decreased, and the cooling rate increased. At high scanning speeds, the ability to form amorphous structures significantly improved, resulting in a refined microstructure, an increased volume fraction of the amorphous phase, and a significant enhancement in the hardness of the laser-cladded coating. The peak hardness at the top of the coating was observed to reach up to 1215.9 $HV_{0.1}$. Sun et al. [85] demonstrated that as the scanning speed increases, the product of the G*R (temperature gradient * grain growth rate) in B-containing Cr17Ni2 coatings also increases, resulting in finer lath martensite and Cr2B phases and, consequently, higher coating hardness.

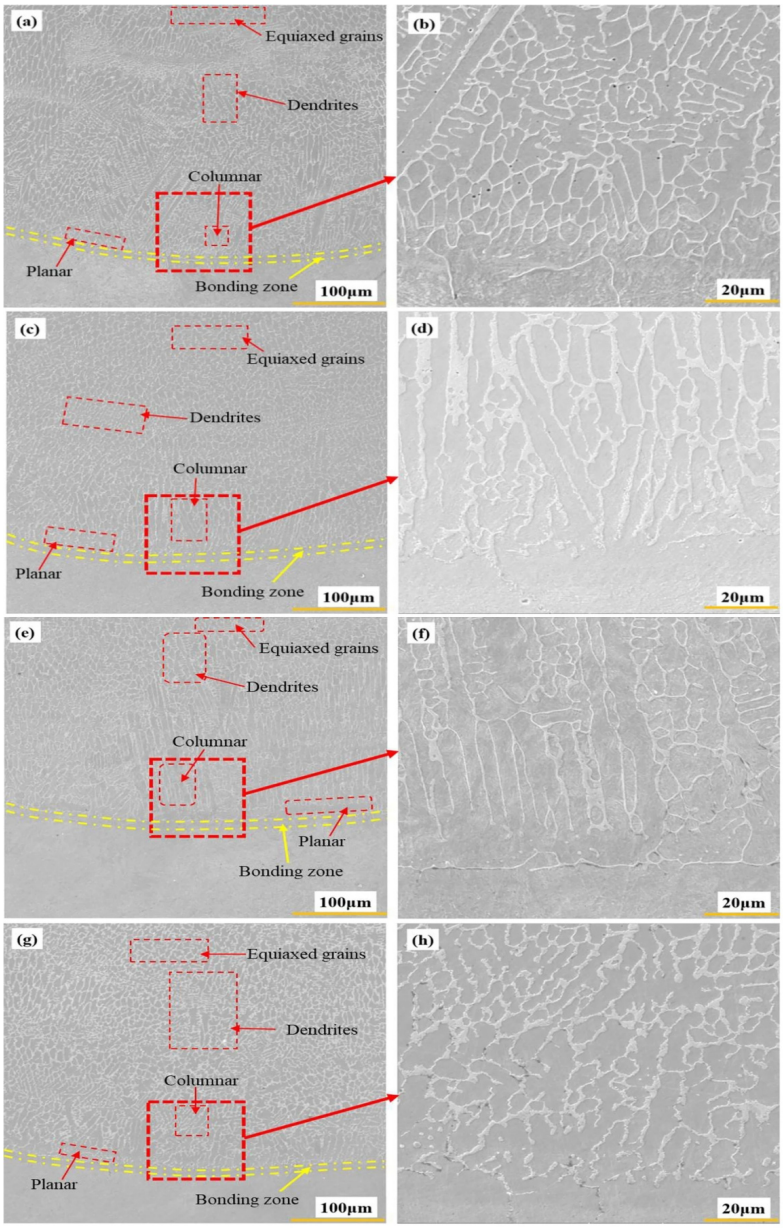

Figure 5. Microstructure of cladding layer at different laser powers: (**a**,**b**) 1.5 kW; (**c**,**d**) 1.8 kW; (**e**,**f**) 2.1 kW; and (**g**,**h**) 2.4 kW [82].

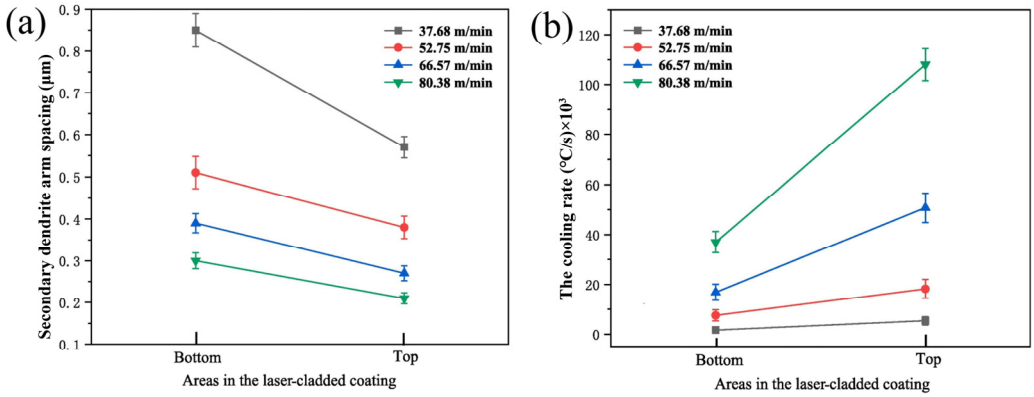

Figure 6. Distance between secondary dendrite arms (**a**) and the cooling rate (**b**) of the coating during laser cladding at varying scanning speeds [84].

3.3. Powder Feed Rate

The powder feed rate refers to the mass of powder introduced into the melt pool per unit time. Selecting an appropriate powder feed rate can mitigate issues such as powder accumulation, uneven heating, and excessive sintering. Wang et al. [86] employed a high-speed powder feeding method to fabricate an iron-based alloy coating on a 27SiMn steel substrate. Compared to the conventional gravity powder feeding (25 g/min), the microstructure of the coating developed through high-speed powder feeding (60 g/min) transitioned from coarse columnar crystals to uniformly distributed small grains. The total energy consumption was only 75.5% of that required by the gravity powder feeding process, allowing for efficient coating production at reduced energy levels. The grain refinement contributed to an increased hardness and improved wear resistance of the coating. Bartkowski et al. [87] prepared Fe/WC metal matrix composite coatings on low-carbon steel surfaces using two distinct powder feed rates (6.25 g/min and 12.5 g/min). At lower powder feed rates, as the laser power increased, the number of cracks decreased, with microhardness values ranging between 1150 $HV_{0.1}$ and 1200 $HV_{0.1}$. In contrast, higher powder feed rates led to increased coating thickness with no observed cracks and microhardness values ranging from 1200 $HV_{0.1}$ to 1400 $HV_{0.1}$. Budde et al. [88] studied the effects of process parameters on the geometry and process stability in laser hot-wire cladding of AISI 52100, finding that a lower wire feed rate (1.5 m/min) resulted in a more stable geometry compared to a higher feed rate (2 m/min).

3.4. Coverage of Shielding Gas

By creating a protective atmosphere, the shielding gas is employed to prevent oxidation and the intrusion of other harmful gasses into the processing space, thereby reducing pore formation and enhancing the density and uniformity of the overlay layer. To effectively avoid unacceptable oxidation during the cladding process, the dimensions of the area sufficiently covered with shielding gas are relevant. This area is referred to as the "effective protective region" [89]. The effective protection region was defined by Ding et al. [90] and Li et al. [89] as the area in which oxygen concentration was below 2000 ppm. The influence of the shielding gas coverage on the laser hot-wire cladding process of high-carbon cladding material AISI 52100 was investigated by Budde et al. [91]. It was found that an increased shielding gas coverage resulted in a reduced ablation rate of alloying elements and fewer pores, along with a nearly halved average dilution rate. The average hardness of the cladding layer was significantly increased. Bernauer et al. [92] designed a new local shielding gas nozzle based on fluid dynamics principles. Through simulations, they explored how the gas flow rate influences gas coverage, finding that an increase in the flow rate can expand the coverage area of the shielding gas.

3.5. Process Parameter Optimization

It is noteworthy that the actual laser cladding process is influenced by the combined effects of multiple parameters, whose interactions contribute to the complex nonlinear relationship between the process parameters and the quality of the cladded layer. Extensive experimentation is often required to optimize these parameters to achieve a high-quality and high-performance cladding layer.

Du et al. [93] adjusted the laser specific energy E_s ($E_s = P/(DV)$, where E_s (J/mm^2) is the laser specific energy, P (W) is the laser power, D (mm) is the spot diameter, and V (mm/s) is the scanning speed) by changing the laser power and scanning speed, and found that with the increase in the specific laser energy, the undercooling degree of Fe60 coating increased during the solidification process, the nucleation rate accelerated, the coating grains became finer and more uniform, and the coating hardness reached 744.2 $HV_{0.2}$. Through the multi-objective optimization of the process parameters of 17-4PH/B4C coating via multilayer laser cladding, Luo et al. [94] found that the factors influencing coating hardness in order of significance are powder feed rate > overlap rate > laser power > scanning speed. The cladding layer produced with the optimal parameters exhibited a microhardness of 784.5 $HV_{0.2}$, approximately four times higher than that of the substrate. Patrycja Wołosz et al. [95] found that the refinement of the microstructure in H13 coatings depends on the scanning speed and the size of the laser spot. The highest hardness achieved under different process parameters reached 800 $HV_{0.1}$. Due to the rapid heating and cooling characteristics of laser cladding, the molten pool exists for a very short duration, resulting in complex interactions among the process parameters. As a result, relying solely on the optimization of process parameters to control the microstructure and properties of the coating has certain limitations. Reddy et al. [96] optimized the process parameters for the laser cladding of SHS7170 iron-based alloy coatings and found that the porosity of the coatings was independent of the process parameters, being primarily determined by the cladding material.

4. External Field-Assisted Treatments

Reasonable cladding material design and the optimization of cladding process parameters can reduce the defects in the coating to a certain extent, but it is still difficult to completely eliminate the cracks and other defects in the microstructure of the high-hardness iron-based coating. In recent years, researchers have combined the external field-assisted technology with laser cladding technology. Through the application of heat treatment, ultrasonic vibration field, electromagnetic field, and other energy fields (as shown in Figure 7), the convection movement of melt is affected, and the temperature field and solute distribution are more uniform. These technologies have played an important role in tissue refinement, defect elimination, and performance improvement.

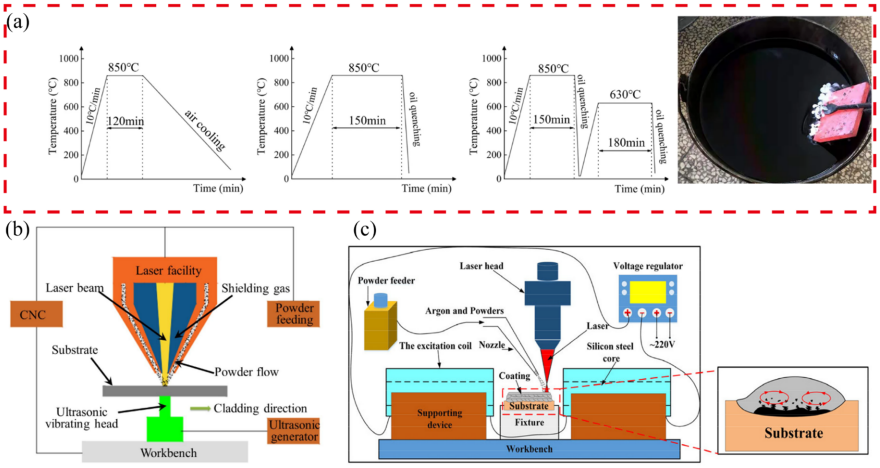

Figure 7. Schematic illustration the heat treatment processes and quenching process (**a**) [97], induction heating-assisted laser cladding (**b**) [98], and electromagnetic field-assisted laser cladding (**c**) [99].

4.1. Heat Treatment Assistance

Heat treatment is a material processing technique that uses controlled heating and cooling to induce phase transformations or structural changes in the solid state. The primary goal is to improve material properties. Strategies such as simultaneous heating and post-heating systems on substrates have been employed for this purpose. The use of tempering, diffusion annealing, and other heat treatment techniques facilitate the diffusion of alloying elements, promoting a more uniform distribution. This approach aids in mitigating the high residual stresses typically encountered during the laser cladding process, ultimately optimizing and enhancing the microstructure and performance of the cladding layer. Wang et al. [100] investigated the mechanisms of post-heat treatment and deep cooling treatment to improve the microhardness of martensitic stainless steel coatings. In the post-heat treatment phase, $Cr_{23}C_6$ particles precipitated from the austenite, leading to diminished levels of C and Cr content. This spurred the formation of martensite, raising the hardness to 700 HV_1. A subsequent deep cooling treatment triggered a phase transition to martensite, further reducing residual austenite content and elevating the coating's hardness to 760 HV_1. Guo et al. [101] employed laser cladding technology to produce Fe60 coatings on a C45E4 steel substrate. They heated the coating to 1050 °C and sustained this temperature for 30 min, followed by cooling in ambient air. This heat treatment process released residual stresses and carbon atoms within the body-centered cubic lattice structure, decreasing deformation and susceptibility to cracks. While the microhardness dropped from 800 HV_1 before the heat treatment to 650 HV_1 after it, the precipitation hardening effect from newly formed carbide particles in the dendrites increased the coating's ultimate tensile strength from 450 MPa to 550 MPa. Gong et al. [102] subjected FeCrNi laser-cladded coatings to heat treatment in the temperature range of 800 °C to 1000 °C. Their findings indicated grain refinement within the coating and the effective elimination of the softening region. This led to a notable enhancement in the tensile strength of the laser-cladded components.

By adjusting laser scanning strategies, in situ laser heat treatment can be achieved. Shi et al. [103] introduced laser idle time between each cladding track, as illustrated in Figure 8, to control the in situ quenching and tempering sequence. The laser idle time between tracks allows the previous track to cool to near room temperature, facilitating a complete martensitic transformation. Consequently, in situ tempering occurs when overlapping tracks pass through. Compared to the 300M steel substrate material, the overall tensile properties of the Δt_{track} = 80 s sample were restored, with a 38% increase in ductility. The yield strength and maximum tensile strength decreased only by 5%–10%, and the wear rate was substantially reduced, yielding excellent overall performance. Gao et al. [104] conducted high-speed re-melting experiments on a titanium-doped iron-based alloy coating, achieving the refinement of the coating. As the re-melting scan speed increased, both the area of the refinement zone and grain size significantly decreased. Rashid et al. [105] utilized laser reheat post-treatment (LPHT) to repair 300 M high-strength steel cladding layers. They found that $M_{23}C_6$ carbides, present in the as-deposited state, dissolved into the martensitic matrix. This led to an increase in the volume of residual austenite and a minor decline in cladding layer hardness. However, the additional laser re-heating of the cladding layer resulted in a uniform distribution of tempered martensite, eliminating localized tempering caused by overlap between passes. LPHT can be effectively employed for the localized control of the microstructure in the laser-cladded repaired parts by tuning the laser reheat parameters. Compared to traditional heat treatment processes, methods such as laser quenching and laser re-melting are more suitable for localized heat treatment requirements. These methods not only significantly shorten the processing cycle but also avoid issues of deformation and high energy consumption that are typical of overall heat treatment processes.

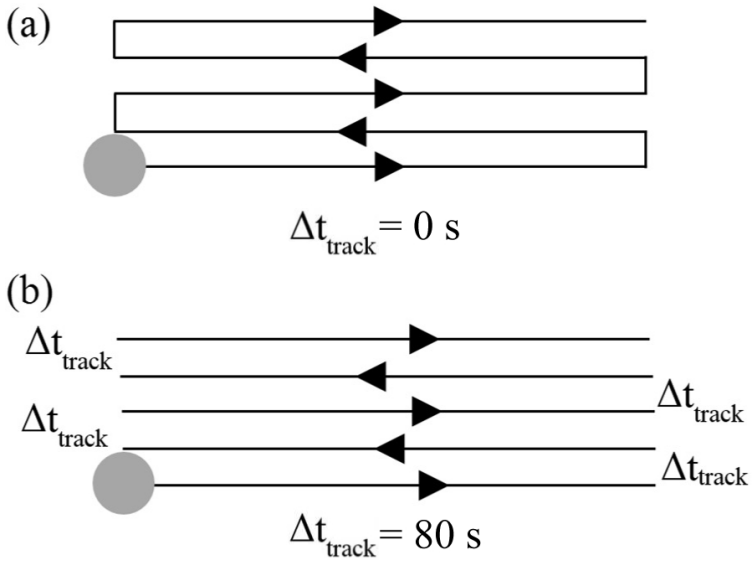

Figure 8. Scan paths with different idle times: (**a**) continuous deposit; (**b**) deposit with a laser idle time of 80 s [103].

4.2. Ultrasonic Vibration Assistance

Ultrasonic vibration-assisted laser cladding technology leverages the synergistic effects of ultrasonic cavitation and acoustic streaming. These effects influence the liquid-phase flow and temperature field distribution within the molten pool, thereby regulating the microstructure and element distribution of the coating [106,107]. Implementing ultrasonic vibration improves the flowability of the liquid metal [108], decreasing the incidence of porosity defects caused by material evaporation and molten pool collapse. It also reduces the temperature gradient within the coating, alleviates thermal stresses, and addresses crack defects [109]. Concurrently, this technology can fragment columnar dendrites, resulting in a finer and more uniformly distributed coating structure [110].

Xu et al. [111] applied ultrasonic vibration assistance during the laser cladding process to deposit an Fe901 alloy coating onto the surface of GCr15 bearing steel. Their results indicated that with the application of ultrasonic vibration, the growth of columnar grains was disrupted, leading to the formation of fine equiaxed grains in the coating. This application of ultrasonic vibration increased the microhardness from 742.6 $HV_{0.2}$ to 783.8 $HV_{0.2}$ and notably reduced the friction coefficient. Xiao et al. [98] utilized laser cladding equipment, as depicted in Figure 7b, to produce $Fe_{41}Co_7Cr_{15}Mo_{14}C_{15}B_6Y_2$ amorphous coatings both with and without ultrasonic vibration. Although the top microhardness of both coatings was similar (approximately 1100 $HV_{0.2}$), the application of ultrasonic vibration increased the thickness of the crystalline region at the bottom of the coating by 46 μm, resulting in a wavy distribution. Furthermore, the microhardness of the transition zone increased by 75 μm. Yao et al. [112] integrated ultrasound into the laser cladding process and identified that the ultrasound significantly reduced the local aggregation of WC particles, promoting a more uniform distribution of WC particles and suppressing crack initiation. Wang et al. [113] examined the properties of 3540Fe/CeO_2 alloy coatings prepared via laser cladding with varying ultrasonic vibration angles. The study revealed that the cladding layer's microstructure, when aided by ultrasonic vibration, consisted of fine equiaxed grains and dendrites, indicating a substantial improvement in grain structure refinement. When subjected to a 45° ultrasonic vibration, the coating's surface appeared smooth and devoid of defects such as cracks and pores, and exhibited the highest average microhardness, reaching 1148 $HV_{0.1}$. This had a significant positive impact on wear resistance.

Excessive energy absorbed by the molten pool due to ultrasonic vibration can prolong its solidification time, leading to grain growth and the formation of coarser grains. Liu et al. [114] observed that ultrasonic power exerted a nonlinear effect on the coating's microstructure. Within a suitable range of ultrasonic power, the grain refinement in the cladding layer was significant. However, when the power exceeded 750 W, the grain size increased. From the studies mentioned, it is evident that alterations in ultrasonic vibration process parameters can influence the microstructure of the cladding layer. By optimizing ultrasonic vibration process parameters in conjunction with laser cladding process parameters, the surface performance of the coating can be further improved. However, this requires further in-depth theoretical and experimental research.

4.3. Electromagnetic Field Assistance

Electromagnetic field-assisted laser cladding technology leverages the interaction between an electromagnetic field and the metal melt, generating electromagnetic forces that alter the convective motion and the processes of heat and mass transfer within the melt. This, in turn, affects the solidification process, leading to a reduction in supercooling and the refinement of the solidified microstructure [115,116]. The electromagnetic field assistance can be categorized into three main types: single magnetic fields (including steady-state, alternating, and rotating magnetic fields), single electric fields (including direct current, alternating current, and pulsed electric fields), and combined electromagnetic fields, each with various configurations.

Ouyang et al. [117] observed that applying an electrostatic field opposite to the laser scanning direction (Figure 9c) can enhance the diffusion and convection of elements within the molten pool, thereby promoting the directional solidification of the laser cladding layer and resulting in the formation of columnar grains. Conversely, applying an electrostatic field aligned with the laser scanning direction (Figure 9d) was found to suppress the diffusion and convection of elements in the molten pool, leading to an orderly mushy solidification and the development of an ultrafine grain structure in the cladding layer. Li et al. [118] established a three-dimensional numerical model for magnetic field-assisted laser cladding, which included chemical species transport, magnetic fields, fluid flow, heat transfer, and dynamic networks. As shown in Figure 10, when the induced magnetic field force and convection velocity acted in opposite directions (Figure 10(a2)), the addition of the magnetic field restricted the flow of the molten metal toward the edges of the molten pool, shortened the length and duration of the molten metal, and increased the maximum cooling rate at the solidification interface (Figure 10(b1–b4)), thus leading to a decrease in grain size. This conclusion was also confirmed by observations of the microstructure in the cladding layer (Figure 10(c1–c3)). Huang et al. [99] utilized electromagnetic field assistance to produce 4 mm thick Fe901 coatings on a $Cr_{12}MoV$ substrate via multilayer laser cladding. The incorporation of the electromagnetic field mitigated cracking defects in the laser-cladded coating. The stirring effect induced by the electromagnetic field disrupted the growth of columnar dendrites, leading to grain refinement and improved the fatigue and wear resistance of the coating. Chen et al. [119] investigated the impact of the electromagnetic field on the microstructure and mechanical properties of $Fe901/Al_2O_3$ metal matrix composite coatings. Their findings highlighted that Lorentz forces, combined with Joule heating effects, increased the nucleation rate of grains, intensified the flow within the molten pool, disrupted the coarse columnar dendrites, and refined the coating structure. The microhardness increased from 782 $HV_{0.2}$ to 866.4 $HV_{0.2}$, and the predominant wear mechanism transitioned from adhesive wear to abrasive wear.

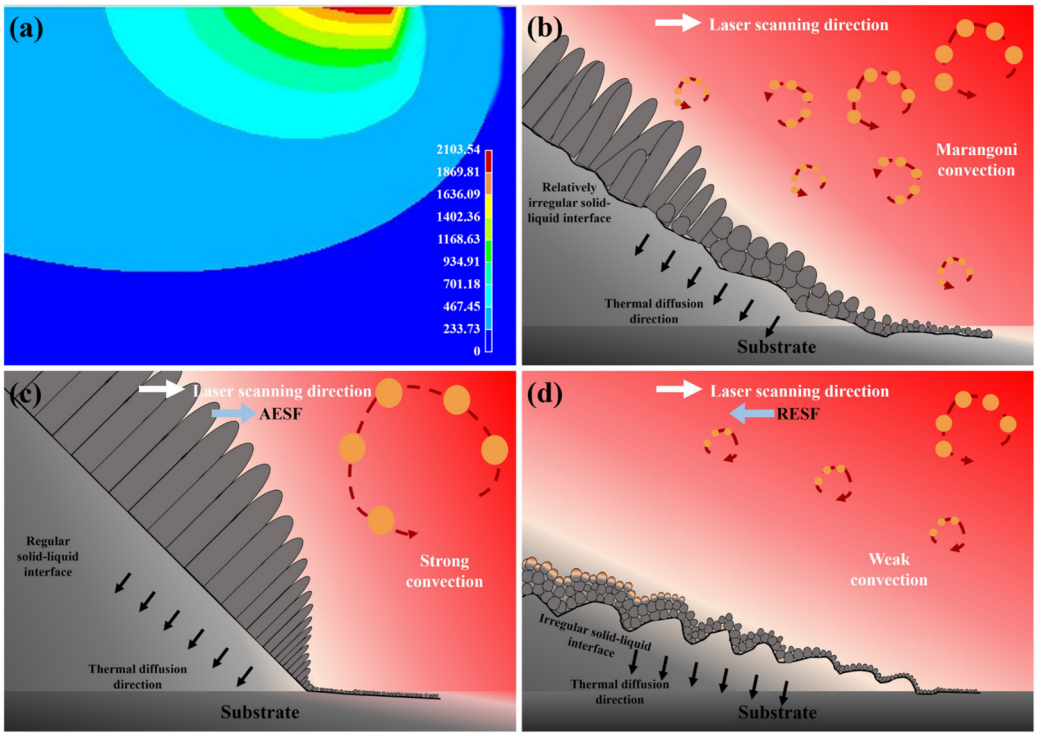

Figure 9. Schematic diagram for the simulated temperature distribution of laser cladding 316 L stainless steel powders (**a**) and schematic diagram showing the crystal growth and convection in the laser cladding layer with different fabrication states (**b**–**d**) [117].

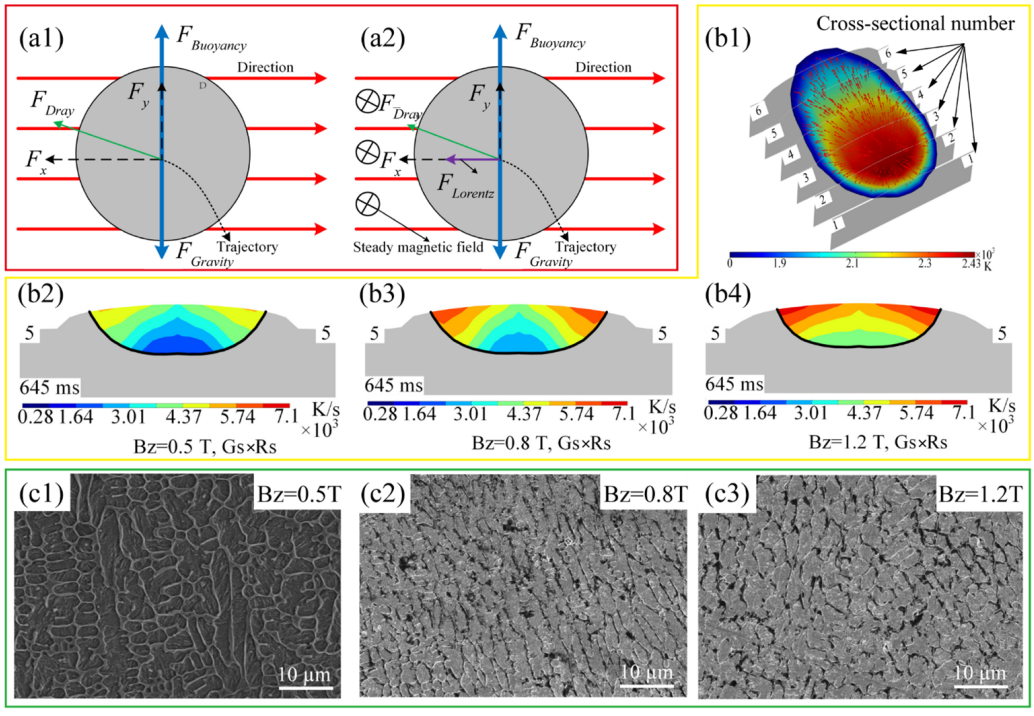

Figure 10. (**a1**,**a2**) Force analysis of melt pool liquid; (**b1**) cross-section positions; (**b2**–**b4**) cross-section cooling rates at different magnetic fields; and (**c1**–**c3**) microstructures at different magnetic fields [118].

4.4. Additive-Equivalent Hybrid Manufacturing

The technology of additive-equivalent hybrid manufacturing introduces mechanical force fields and thermal fields during the additive phase or subsequent post-processing, based on processes such as rolling, forging [120], hammering, and shot peening, to induce

plastic deformation at specific depths within the additive layers. This approach enhances the grain morphology, microstructure, and stress state of the deposited material, enabling effective control over the macroscopic mechanical properties and ultimately improving the fatigue life of the formed materials. Chen et al. [121] prepared Fe-based alloy coatings on a 27SiMn substrate through laser cladding. It was observed that after undergoing ultrasonic high-frequency micro-forging (UH-FM), the surface layer of the coating was broken and refined, and a gradient structure appeared. A part of the fcc phase was transformed into the bcc phase, which increased the resistance of dislocation movement, and the hardness of the coating increased. Cai et al. [122] observed that after rolling, the tops of the columnar grains in the FeCoCrNi alloy coatings produced by laser cladding exhibited increased width and a noticeable inclination. Zhang et al. [123] combined laser deposition technology with shot peening and discovered that the yield strength of the Fe-based alloy coatings produced by this hybrid process was significantly enhanced. Additionally, some coarse columnar grains were refined, leading to a reduction in grain size heterogeneity and an overall improvement in the microstructure.

4.5. Assistance from Multiple Physical Fields

The control effects of single energy fields, such as ultrasonic fields, electromagnetic fields, and thermal fields, on defects like porosity and cracks in the cladding layer each have their advantages in different application areas. However, issues still arise with the beneficial effects produced during the laser cladding process, such as the attenuation of ultrasound during transmission, the complexity of electromagnetic field equipment, and the uneven temperature distribution in thermal fields. The technology of multi physics-assisted laser cladding involves the coupling of various physical energy fields to leverage their synergistic effects, thereby addressing the limitations of single-process techniques and extending the capabilities for the organization and performance regulation of high-hardness iron-based alloy coatings. Zhou et al. [124] developed a preheating and ultrasonic composite-assisted laser additive manufacturing method, comparing the effects of single energy fields and composite energy fields on the microstructure and properties of the 24CrNiMoY coating. It was found that the synergistic effect of the dual fields had a more significant influence on the coating's density, phase composition, grain size, and strength–ductility matching properties. Zheng et al. [125] combined ultrasonic waves with traditional rolling processes to investigate the impact of the hybrid process on the surface quality of Fe-based alloy coatings, comparing it with conventional rolling. It was observed that the coatings produced through the hybrid process exhibited finer grain sizes, with surface roughness reduced to only one-quarter of that of the traditionally rolled coatings, and both hardness and residual compressive stress were found to be higher than those of the coatings subjected to conventional rolling.

5. Conclusions

In recent decades, there has been significant advancement in the preparation of high-hardness iron-based alloy coatings using laser cladding, particularly in terms of cladding material composition, laser processing techniques, and the optimization of coating performance. However, due to persistent issues with coating defects and cost considerations, its broad industrial application remains limited. To realize coatings that exhibit metallurgical bonding with the substrate and deliver satisfactory performance, future research should focus on the areas outlined in Table 3.

Table 3. Future research directions and focus areas.

Improvement Direction	Measures	Expected Performance	Potential Drawbacks
Improvement of iron-based alloy powders	Combining the characteristics of non-equilibrium solidification in laser cladding and considering different reinforcement and repair targets, a database will be established using digital manufacturing technology.	Establishing a predictive model for the relationship between material composition, microstructure, and properties to effectively address the issue of cracking	Extensive experimental validation is still required.
Optimization of process parameters	By integrating digital manufacturing technology, process parameters can be dynamically adjusted through real-time monitoring and feedback systems.	Improving the stability and repeatability of coating quality	It may increase the complexity and cost of the system.
Composite energy field	Exploring the coupling effects of the composite energy field and optimizing the energy field parameters and application methods	Effectively suppressing the generation of defects by extending the limits of coating microstructure and performance control	The specific effects of different energy field parameters are difficult to quantify.

Author Contributions: Conceptualization, methodology, and investigation, L.L. and Y.L.; formal analysis, supervision, and writing—review and editing, Y.L., X.K., L.P. and X.W.; writing—original draft preparation, L.L.; project administration and funding acquisition, Y.L. and X.W. All authors have read and agreed to the published version of the manuscript.

Funding: The research work was financially supported by the Key Technology Innovation and Industrialization Project of Fujian Province (No. 2023XQ017), the Natural Science Foundation of Hunan Province of China (No. 2024JJ5336), the Natural Science Foundation of Hunan Province of China—Provincial and Municipal Joint Fund (No. 2022JJ50019), the Hengyang Guiding Plan Project (No. hyzdxjh202101), and the University of South China Talent Introduction Project (No. 210XQD017).

Institutional Review Board Statement: Not applicable.

Informed Consent Statement: Not applicable.

Data Availability Statement: Data are contained within the manuscript.

Conflicts of Interest: Author Longsheng Peng was employed by Hunan Lifang Roller Co., Ltd. The remaining authors declare that the research was conducted in the absence of any commercial or financial relationships that could be construed as a potential conflict of interest.

References

1. Shi, Y.; Xia, Q.; Xie, M.; Zhou, Q.; Hua, D.; Chai, L.; Shi, T.; Eder, S.J.; Wang, H.; Wang, P.; et al. Insights into irradiation-affected structural evolution and mechanical behavior of amorphous carbon. *Acta Mater.* **2024**, *281*, 120424. [CrossRef]
2. Zhou, Q.; Luo, D.; Hua, D.; Ye, W.; Li, S.; Zou, Q.; Chen, Z.; Wang, H. Design and characterization of metallic glass/graphene multilayer with excellent nanowear properties. *Friction* **2022**, *10*, 1913–1926. [CrossRef]
3. Li, L.; Yao, C.; Huang, J.; Feng, K.; Li, Z. Characteristics of interdendritic residual austenite in laser cladding of high hardness iron-based coating. *Chin. J. Lasers* **2017**, *44*, 0302011.
4. Trojan, K.; Ocelík, V.; Čapek, J.; Čech, J.; Canelo-Yubero, D.; Ganev, N.; Kolařík, K.; De Hosson, J.T.M. Microstructure and mechanical properties of laser additive manufactured H13 tool steel. *Metals* **2022**, *12*, 243. [CrossRef]
5. Shi, X.; Wen, D.; Wang, S.; Wang, G.; Zhang, M.; Liao, J.; Xu, C. Investigation on friction and wear performance of laser cladding Ni-based alloy coating on brake disc. *Optik* **2021**, *242*, 167227. [CrossRef]
6. Pellizzari, M.; Zhao, Z.; Bosetti, P.; Perini, M. Optimizing direct laser metal deposition of H13 cladding on CuBe alloy substrate. *Surf. Coat. Technol.* **2022**, *432*, 128084. [CrossRef]
7. ZuoJiang, S.; Yu, H.; Jiang, X.; Gao, W.; Sun, D. A thermal field FEM of titanium alloy coating on low-carbon steel by laser cladding with experimental validation. *Surf. Coat. Technol.* **2022**, *452*, 129113. [CrossRef]
8. Wang, J.; Timokhina, I.; Sharp, K.; Shekhter, A.; Liu, Q. Microstructure and precipitation behaviours of laser clad 7075 aluminium alloy. *Surf. Coat. Technol.* **2022**, *445*, 128726. [CrossRef]

9. Zhu, L.; Xue, P.; Lan, Q.; Meng, G.; Ren, Y.; Yang, Z.; Xu, P.; Liu, Z. Recent research and development status of laser cladding: A review. *Opt. Laser Technol.* **2021**, *138*, 106915. [CrossRef]
10. Dmitrieva, A.; Klimova-Korsmik, O.; Gushchina, M.O.; Korsmik, R.; Zadykyan, G.; Tukov, S. Effect of the laser cladding parameters on the crack formation and microstructure during nickel superalloy gas turbine engines repair. *Metals* **2023**, *13*, 393. [CrossRef]
11. Ritchie, R.O. The conflicts between strength and toughness. *Nat. Mater.* **2011**, *10*, 817–822. [CrossRef] [PubMed]
12. Ouyang, C.; Wang, R.; Bai, Q.; Chen, Z.; Yan, X. Aging strengthening treatment of laser cladding Co-based alloy coating. *Mater. Lett.* **2022**, *313*, 131746. [CrossRef]
13. Awasthi, R.; Limaye, P.K.; Kumar, S.; Kushwaha, R.P.; Viswanadham, C.S.; Srivastava, D.; Soni, N.L.; Patel, R.J.; Dey, G.K. Wear characteristics of Ni-based hardfacing alloy deposited on stainless steel substrate by laser cladding. *Metall. Mater. Trans. A* **2015**, *46*, 1237. [CrossRef]
14. Wang, C.; Wang, W.; Ding, S.; Gong, P.; Gao, Y. Preparation and tribological properties of laser cladding iron based wear resistant coatings. *Chin. J. Lasers* **2022**, *49*, 137–147.
15. Yang, Y.-l.; Zhou, L.-l.; Chen, H.-b.; Wang, J.; Qiao, H.C.; Lu, Y.; Qin, G.-w. Laser shock peening Fe-based coatings for enhancing wear and corrosion resistance. *Mater. Sci. Technol.* **2021**, *37*, 1214–1224. [CrossRef]
16. Yang, P.; Song, Y.; Wang, J.; Hu, F.; Xie, L. Semiconductor laser cladding of an Fe-based alloy on nodular cast iron. *Weld. World* **2021**, *65*, 785–792. [CrossRef]
17. Ding, H.; Mu, X.; Zhu, Y.; Yang, W.; Xiao, Q.; Wang, W.; Liu, Q.; Guo, J.; Zhou, Z. Effect of laser claddings of Fe-based alloy powder with different concentrations of WS2 on the mechanical and tribological properties of railway wheel. *Wear* **2022**, *488–489*, 204174. [CrossRef]
18. Xie, Z.; Liu, C.; Wu, Q.; Chen, S.; Liang, J. A review on the preparation of high hard and wear resistant coatings by laser cladding. *Surf. Technol.* **2022**, *52*, 25–40.
19. Li, Q.; Fu, H. Research progress in laser cladding of iron based wear-resistant alloys. *J. B. Univ. Technol.* **2013**, *39*, 1552–1560.
20. Aghasibeig, M.; Fredriksson, H. Laser cladding of a featureless iron-based alloy. *Surf. Coat. Technol.* **2012**, *209*, 32–37. [CrossRef]
21. Feng, K.; Guo, Y.; Feng, Y.; Yao, C.; Zhu, Y.; Zhang, Q.; Li, Z. Microstructure controlling and properties of laser cladded high strength and high toughness Fe-based coatings. *Acta Metall. Sin. Engl. Lett.* **2022**, *58*, 513–528.
22. Jiang, M.; Sun, S.; Wang, J.; Wang, P.; Sun, X.; Shao, J.; Liu, J.; Cao, A.; Sun, W.; Chen, X. Research progress in wear resistance of high entropy alloy coatings prepared by laser cladding. *J. Mater. Eng.* **2022**, *50*, 18–32.
23. Zhou, Q.; Jiao, Z.; Huang, Z.; Shi, Y.; Li, Y.; Ying, C.; Wang, H.; Cavalcanti Pinto, H.; Greiner, C.; Liu, W. Wear-resistant CrCoNi nanocrystalline film via friction-driven surface segregation. *Acta Mater.* **2024**, *279*, 120299. [CrossRef]
24. Lentz, J.; Röttger, A.; Theisen, W. Mechanism of the $Fe_3(B, C)$ and $Fe_{23}(C, B)_6$ solid-state transformation in the hypoeutectic region of the Fe-C-B system. *Acta Mater.* **2016**, *119*, 80–91. [CrossRef]
25. Lentz, J.; Röttger, A.; Theisen, W. Hardness and modulus of Fe_2B, $Fe_3(C, B)$, and $Fe_{23}(C, B)_6$ borides and carboborides in the Fe-C-B system. *Mater. Charact.* **2018**, *135*, 192–202. [CrossRef]
26. Dong, G.; You, H.; Mao, K.; Yuan, N.; Ge, M.; Yu, X.; Zhang, Q.; Yao, J. Effect of Si element content on the manufacturing process and corrosion performance of laser clad 316L. *Surf. Technol.* **2024**, *53*, 179–190.
27. Li, Q.; Wang, Q.; Zhang, L.; Chen, D.; Jin, H.; Li, J.; Zhang, J. Microstructure, wear and electrochemical behaviors of laser cladding Fe-based coatings with various molybdenum contents. *Mater. Res. Express* **2022**, *9*, 026504. [CrossRef]
28. Liu, X.; Wang, H.; Liu, Y.; Wang, C.; Song, Q.; Cui, H.; Zhang, C.; Huang, K. The effect of Nb content on microstructure and properties of laser cladding 316L SS coating. *Surf. Coat. Technol.* **2021**, *425*, 127684. [CrossRef]
29. Yang, Y.; Xing, Y.; Chen, H.; Liu, Z.; Wang, B.; Qiao, H.; Zhang, E. Improving wear and corrosion resistance of U71Mn rail steel subjected to laser in-situ fabrication of Fe based Cr–V coatings. *Wear* **2024**, *546–547*, 205312. [CrossRef]
30. Yang, J.; Miao, X.; Wang, X.; Yang, F. Influence of Mn additions on the microstructure and magnetic properties of FeNiCr/60% WC composite coating produced by laser cladding. *Int. J. Refract. Hard. Met.* **2014**, *46*, 58–64. [CrossRef]
31. Shang, F.; Xu, Z.; Chen, J.; Chen, L.; Lu, S.; Wang, S.; Jing, X.; Dubovyi, O. Effect of Cr on wear resistance and mechanism of preset-powder laser cladding T15 alloy steel coating. *J. Mater. Res. Technol.* **2024**, *29*, 4991–4999. [CrossRef]
32. Feng, Y.; Pang, X.; Feng, K.; Feng, Y.; Li, Z. Study on microstructure and compressive properties of Fe-C-W-Cr-V-Nb coating with boron addition. *J. Alloys Compd.* **2022**, *904*, 163986. [CrossRef]
33. Wang, Q.; Bai, X.; Sun, B.; Liu, J.; Cai, Z.; Liang, X.; Shen, B. Influence of Si on tribological behavior of laser cladded Fe-based amorphous/crystalline composite coatings. *Surf. Coat. Technol.* **2021**, *405*, 126570. [CrossRef]
34. Liang, Z.; Zhan, J.; Shi, W.; Xie, Y.; Huang, J.; An, F. The effect of Si addition amount on Fe-based alloy laser cladding coating. *Appl. Laser* **2020**, *40*, 593–597.
35. Chen, K.; Yang, X.; Li, W.; Xia, G.; Wang, S.; Wang, K. Study on the wear and corrosion resistance of Fe–Mo coatings on 65Mn steel ploughshares by laser cladding. *Appl. Phys. A* **2022**, *128*, 795. [CrossRef]
36. Cao, S.; Liang, J.; Zhou, J. Evolution in microstructure features and properties of Mo-containing Fe-Cr-Ni-B-Si composite coatings by laser cladding. *Mater. Charact.* **2022**, *188*, 111926. [CrossRef]
37. Ma, X.; Wang, K.; Fu, H.; Ju, J.; Lei, Y.; Yi, D. Effect of Mo content on microstructure and properties of laser cladding Fe-based alloy coatings. *Surf. Rev. Lett.* **2018**, *25*, 1850077.

38. Wang, H.Z.; Cheng, Y.H.; Yang, J.Y.; Wang, Q.Q. Microstructure and properties of laser clad Fe-based amorphous alloy coatings containing Nb powder. *J. Non-Cryst. Solids* **2020**, *550*, 120351. [CrossRef]
39. Shan, B.; Chen, J.; Chen, S.; Ma, M.; Ni, L.; Shang, F.; Zhou, L. Laser cladding of Fe-based corrosion and wear-resistant alloy: Genetic design, microstructure, and properties. *Surf. Coat. Technol.* **2022**, *433*, 128117. [CrossRef]
40. Yao, C.; Xu, B.; Huang, J.; Zhang, P.; Li, Z.; Wu, Y. Microstructure design of controlling crack of Fe-based laser cladding layer. *China Surf. Eng.* **2010**, *23*, 74–79+83.
41. Chen, L.; Lan, Y.; Cheng, Y.; Zeng, J.; Ma, Y.; Yu, S.; Ding, Z.; Liu, B.; Zhang, J.; Peng, H.; et al. Friction behavior and wear mechanism of laser cladded FeNiCr-WC composite coatings in comparison with different friction pairs. *J. Mater. Res. Technol.* **2024**, *31*, 1956–1973. [CrossRef]
42. Zhang, X.; Lu, W.; Guo, H.; Huo, F.; Chen, H.; Qiu, K.; Yang, B.; Wang, J. Effect of WC–Co addition on tribological and cracking behavior of laser cladded Fe-based amorphous/crystalline composite coatings. *J. Mater. Sci.* **2023**, *58*, 11804–11819. [CrossRef]
43. Liu, C.; Xu, P.; Pang, C.; Zha, G.; Ouyang, Z.; Chen, J. Phase transformation in Fe–Mn–Si SMA/WC composite coating developed by laser cladding. *Mater. Chem. Phys.* **2021**, *267*, 124595. [CrossRef]
44. Li, J.; Zhu, Z.; Peng, Y.; Shen, G. Phase evolution and wear resistance of in-situ synthesized (Cr, W)23C6-WC composite ceramics reinforced Fe-based composite coatings produced by laser cladding. *Vacuum* **2021**, *190*, 110242. [CrossRef]
45. Xu, N.; Zhang, Q.; Yao, J. Microstructure of in-site synthesis TiC hardened coating by laser irradiation. *Chin. J. Lasers* **2010**, *37*, 2653–2657.
46. Zhang, Z.; Wang, X.; Zhang, Q.; Liang, Y.; Ren, L.; Li, X. Fabrication of Fe-based composite coatings reinforced by TiC particles and its microstructure and wear resistance of 40Cr gear steel by low energy pulsed laser cladding. *Opt. Laser Technol.* **2019**, *119*, 105622. [CrossRef]
47. Li, A.; Wei, C.; Liu, J.; Zhou, W.; Wang, H.; Kuang, S. Microstructure, friction and wear properties of laser cladding Fe-based Cr_3C_2/MoS_2 coatings. *China Surf. Eng.* **2015**, *28*, 77–85.
48. Li, H.; Gao, Q.; Li, K.; Li, B. Properties of surface laser cladding H13/NiCr-Cr3C2 composite powder cladding layer. *Chin. J. Lasers* **2018**, *48*, 163–172.
49. Chen, L.; Yu, T.; Xu, P.; Zhang, B. In-situ NbC reinforced Fe-based coating by laser cladding: Simulation and experiment. *Surf. Coat. Technol.* **2021**, *412*, 127027. [CrossRef]
50. Aramide, B.; Jamiru, T.; Pityana, S.; Sadiku, R.; Popoola, P. Scanning speed effect on the microstructure, hardness, wear, and corrosion performance of VC-Cr3C2 reinforced laser claddings on steel baseplate for tillage application. *Trans. Indian Inst. Met.* **2022**, *75*, 2149–2157. [CrossRef]
51. Tan, H.; Luo, Z.; Li, Y.; Yan, F.; Duan, R. Microstructure and wear resistance of Al2O3–M7C3/Fe composite coatings produced by laser controlled reactive synthesis. *Opt. Laser Technol.* **2015**, *68*, 11–17. [CrossRef]
52. Fomin, V.M.; Malikov, A.G.; Golyshev, A.A.; Bulina, N.V.; Gulov, M.A.; Vitoshkin, I.E.; Brusentseva, T.A.; Filippov, A.A.; Mishin, A.V. Structural-phase state and mechanical properties of a laser cladding titanium matrix composite based on Ti64 alloy and TiB2 ceramics. *Phys. Mesomech.* **2024**, *27*, 1–15. [CrossRef]
53. Naizabekov, A.; Samodurova, M.; Bodrov, E.; Lezhnev, S.; Samoilova, O.; Trofimov, E.; Mikhailov, D.; Litvinyuk, K.; Trofimova, S.; Latfulina, Y.; et al. Use of laser cladding for the synthesis of coatings from high-entropy alloys reinforced with ceramic particles. *Case Stud. Constr. Mater.* **2023**, *19*, e02541. [CrossRef]
54. Wang, J.; Li, L.; Tao, W. Crack initiation and propagation behavior of WC particles reinforced Fe-based metal matrix composite produced by laser melting deposition. *Opt. Laser Technol.* **2016**, *82*, 170–182. [CrossRef]
55. Li, W.; Yang, X.; Wang, S.; Duan, D.; Li, F.; Qiao, Y.; Liu, Y.; Liu, X. The effect of WC content on the bonding strength and mechanical properties of WC/Ni60 coatings of brake disc. *Opt. Laser Technol.* **2022**, *149*, 107822. [CrossRef]
56. Lu, J.Z.; Cao, J.; Lu, H.F.; Zhang, L.Y.; Luo, K.Y. Wear properties and microstructural analyses of Fe-based coatings with various WC contents on H13 die steel by laser cladding. *Surf. Coat. Technol.* **2019**, *369*, 228–237. [CrossRef]
57. Zhu, H.; Ouyang, M.; Hu, J.; Zhang, J.; Qiu, C. Design and development of TiC-reinforced 410 martensitic stainless steel coatings fabricated by laser cladding. *Ceram. Int.* **2021**, *47*, 12505–12513. [CrossRef]
58. Li, J.; Zhu, Z.; Peng, Y.; Shen, G. A comparative study on microstructure evolution and wear resistance of different-sized tungsten carbide modified Fe-based laser cladding coatings. *Opt. Laser Technol.* **2022**, *147*, 107672. [CrossRef]
59. Xiao, Q.; Sun, W.l.; Yang, K.x.; Xing, X.f.; Chen, Z.h.; Zhou, H.n.; Lu, J. Wear mechanisms and micro-evaluation on WC particles investigation of WC-Fe composite coatings fabricated by laser cladding. *Surf. Coat. Technol.* **2021**, *420*, 127341. [CrossRef]
60. Zou, L.; Liu, X.; Wang, L.; Xie, H.; Cai, Y. Effects of cast tungsten carbide powder on wear resistance of laser cladding ceramic particle reinforced iron matrix composite. *Rare Met. Mater. Eng.* **2017**, *46*, 1126–1131.
61. Chen, T.; Deng, Z.; Liu, D.; Zhu, X.; Xiong, Y. Bioinert TiC ceramic coating prepared by laser cladding: Microstructures, wear resistance, and cytocompatibility of the coating. *Surf. Coat. Technol.* **2021**, *423*, 127635. [CrossRef]
62. Xu, L.; Xiao, R.; Qu, G.; Wang, D. In situ synthesized graded TiC particulate reinforced Ni-based composite coating prepared by laser cladding. *J. Phys. Conf. Ser.* **2021**, *1820*, 012050. [CrossRef]
63. Richardson, P.; Cuskelly, D.; Brandt, M.; Kisi, E. Microstructural analysis of in-situ reacted Ti2AlC MAX phase composite coating by laser cladding. *Surf. Coat. Technol.* **2020**, *385*, 125360. [CrossRef]
64. Adesina, O.S.; Popoola, A.P.I.; Pityana, S.L.; Oloruntoba, D.T. Microstructural and tribological behavior of in situ synthesized Ti/Co coatings on Ti-6Al-4V alloy using laser surface cladding technique. *Int. J. Adv. Manuf. Tech.* **2018**, *95*, 1265–1280. [CrossRef]

65. Ren, Y.; Li, L.; Zhou, Y.; Wang, S. In situ synthesized VC reinforced Fe-based coating by using extreme high-speed laser cladding. *Mater. Lett.* **2022**, *315*, 131962. [CrossRef]
66. Weng, F.; Yu, H.; Chen, C.; Liu, J.; Zhao, L.; Dai, J. Fabrication of Co-based coatings on titanium alloy by laser cladding with CeO_2 addition. *Mater. Manuf. Process.* **2016**, *31*, 1461–1467. [CrossRef]
67. Zhu, Z.; Li, J.; Peng, Y.; Shen, G. In-situ synthesized novel eyeball-like Al_2O_3/TiC composite ceramics reinforced Fe-based alloy coating produced by laser cladding. *Surf. Coat. Technol.* **2020**, *391*, 125671. [CrossRef]
68. Mohammed, S.; Balu, P.; Ahmed, A.; Zhang, Z.; Kovacevic, R. Improvement of wear resistance of the nickel based alloy mixed with rare earth elements by high power direct diode laser cladding. *Lasers Manuf. Mater. Process.* **2019**, *6*, 173–188. [CrossRef]
69. Das, A.K. Effect of rare earth oxide additive in coating deposited by laser cladding: A review. *Mater. Today Proc.* **2022**, *52*, 1558–1564. [CrossRef]
70. Quazi, M.M.; Fazal, M.A.; Haseeb, A.S.M.A.; Yusof, F.; Masjuki, H.H.; Arslan, A. Effect of rare earth elements and their oxides on tribo-mechanical performance of laser claddings: A review. *J. Rare Earths* **2016**, *34*, 549–564. [CrossRef]
71. Jiang, H.; Zhao, X.; Cao, S.; Wang, D.; Zhu, Q.; Lei, Y. Improvement of the mechanical properties and LBE cavitation erosion resistance of laser cladded FeCrAlTiC coating by Y_2O_3 addition. *Mater. Lett.* **2022**, *326*, 132882. [CrossRef]
72. Wang, Q.; Yang, J.; Niu, W.; Li, Y.; Mao, X.; Wang, Y.; Zhang, K. Effect of La_2O_3 on microstructure and properties of Fe-based alloy coatings by laser cladding. *Optik* **2021**, *245*, 167653. [CrossRef]
73. Cai, Y.; Luo, Z.; Chen, Y.; Ao, S. Influence of CeO_2 on tribological behaviour of TiC/Fe-based composite coating. *Surf. Eng.* **2017**, *33*, 936–943. [CrossRef]
74. Chen, L.; Zhao, Y.; Guan, C.; Yu, T. Effects of CeO_2 addition on microstructure and properties of ceramics reinforced Fe-based coatings by laser cladding. *Int. J. Adv. Manuf. Technol.* **2021**, *115*, 2581–2593. [CrossRef]
75. Zhang, M.; Wang, X.H.; Qu, K.L.; Liu, S.S. Effect of rare earth oxide on microstructure and high temperature oxidation properties of laser cladding coatings on 5CrNiMo die steel substrate. *Opt. Laser Technol.* **2019**, *119*, 105597. [CrossRef]
76. Yu, W.; Ma, P.; Bai, W.; Chen, J. Numerical simulation of temperature field and stress field in 316l/Aisi304 laser cladding with different scanning strategies. *Chin. J. Lasers* **2021**, *48*, 18–29.
77. Fan, S.; Mao, J.; Xie, S.; Wang, L.; Yao, Z.; Chen, Z.; Yao, J. Effect of pulsed/continuous double-beam hybrid laser cladding on microstructure of 316l stainless steel. *Chin. J. Lasers* **2023**, *50*, 80–90.
78. Muvvala, G.; Patra Karmakar, D.; Nath, A.K. Online monitoring of thermo-cycles and its correlation with microstructure in laser cladding of nickel based super alloy. *Opt. Lasers Eng.* **2017**, *88*, 139–152. [CrossRef]
79. Chen, C.; Meiping, W.; Rui, H.; Yuling, G.; Xiaojin, M. Understanding stellite-6 coating prepared by laser cladding: Convection and columnar-to-equiaxed transition. *Opt. Laser Technol.* **2022**, *149*, 107885. [CrossRef]
80. Wang, K.; Liu, W.; Hong, Y.; Sohan, H.M.S.; Tong, Y.; Hu, Y.; Zhang, M.; Zhang, J.; Xiang, D.; Fu, H.; et al. An overview of technological parameter optimization in the case of laser cladding. *Coatings* **2023**, *13*, 496. [CrossRef]
81. Mao, J.; Feng, A.; Cheng, B.; Li, Z.; Wu, H.; Huang, Y.; Zhang, H. Microstructure and friction and wear properties of Fe-based alloy coatings by laser cladding. *Hot Work. Technol.* **2017**, *46*, 139–142.
82. Xie, Y.; Chen, W.; Liang, L.; Huang, B.; Zhuang, J. Influence of laser power on the microstructure and properties of Fe314 alloy cladding layer on EA4T steel. *Weld. World* **2022**, *66*, 1551–1563. [CrossRef]
83. Jiao, X.; Wang, J.; Wang, C.; Gong, Z.; Pang, X.; Xiong, S.M. Effect of laser scanning speed on microstructure and wear properties of T15M cladding coating fabricated by laser cladding technology. *Opt. Lasers Eng.* **2018**, *110*, 163–171. [CrossRef]
84. Li, R.; Yuan, W.; Yue, H.; Zhu, Y. Study on microstructure and properties of Fe-based amorphous composite coating by high-speed laser cladding. *Opt. Laser Technol.* **2022**, *146*, 107574. [CrossRef]
85. Sun, Z.; Du, C.; Yu, Z.; Long, Y.; Ren, X. Effect of cladding speed on the microstructure and hardness of high-hardness B-bearing Cr17Ni2 coating. *J. Mater. Res. Technol.* **2024**, *31*, 668–678. [CrossRef]
86. Wang, Q.; Qian, R.; Yang, J.; Niu, W.; Zhou, L.; Pan, X.; Su, C. Effect of high-speed powder feeding on microstructure and tribological properties of Fe-based coatings by laser cladding. *Coatings* **2021**, *11*, 1456. [CrossRef]
87. Bartkowski, D.; Bartkowska, A.; Jurči, P. Laser cladding process of Fe/WC metal matrix composite coatings on low carbon steel using Yb: YAG disk laser. *Opt. Laser Technol.* **2021**, *136*, 106784. [CrossRef]
88. Budde, L.; Biester, K.; Lammers, M.; Hermsdorf, J.; Kaierle, S.; Overmeyer, L. Influence of process parameters on single weld seam geometry and process stability in Laser Hot-Wire Cladding of AISI 52100. *Adv. Ind. Manuf. Eng.* **2023**, *7*, 100122. [CrossRef]
89. Li, G.; Zhang, J.; Shi, T.; Shi, J.; Cheng, D.; Lu, L.; Shi, S. Experimental investigation on laser metal deposition of Ti-6Al-4V alloy with coaxial local shielding gas nozzle. *J. Mater. Eng. Perform.* **2020**, *29*, 7821–7829. [CrossRef]
90. Ding, J.; Colegrove, P.; Martina, F.; Williams, S.; Wiktorowicz, R.; Palt, M.R. Development of a laminar flow local shielding device for wire + arc additive manufacture. *J. Mater. Process. Technol.* **2015**, *226*, 99–105. [CrossRef]
91. Budde, L.; Biester, K.; Coors, T.; Faqiri, M.Y.; Lammers, M.; Hermsdorf, J.; Hassel, T.; Pape, F.; Overmeyer, L. Influence of shielding gas coverage during laser hot-wire cladding with high carbon steel. *Int. J. Adv. Manuf. Technol.* **2023**, *127*, 3195–3207. [CrossRef]
92. Bernauer, C.; Meinzinger, L.; Zapata, A.; Zhao, X.; Baehr, S.; Zaeh, M.F. Design and investigation of a novel local shielding gas concept for laser metal deposition with coaxial wire feeding. *Appl. Sci.* **2023**, *13*, 5121. [CrossRef]
93. Du, Y.; Peng, Y.; Mao, K.; He, G.; Zhang, L. Effect of laser specific energy on mechanical properties of Fe60 coatings by laser cladding. *Opt. Laser Technol.* **2024**, *172*, 110497. [CrossRef]

94. Luo, D.; Liu, C.; Wang, C.; Wang, Y.; Wang, X.; Zhao, J.; Jiang, S. Optimization of multilayer laser cladding process parameters based on NSGA-II-MOPSO algorithm. *Opt. Laser Technol.* **2024**, *176*, 111025. [CrossRef]
95. Wołosz, P.; Baran, A.; Polański, M. The influence of laser engineered net shaping (LENS™) technological parameters on the laser deposition efficiency and properties of H13 (AISI) steel. *J. Alloys Compd.* **2020**, *823*, 153840. [CrossRef]
96. Reddy, L.; Preston, S.P.; Shipway, P.H.; Davis, C.; Hussain, T. Process parameter optimisation of laser clad iron based alloy: Predictive models of deposition efficiency, porosity and dilution. *Surf. Coat. Technol.* **2018**, *349*, 198–207. [CrossRef]
97. Yingtao, Z.; Yongliang, M.; Gang, W.; Xiulin, J.; Zhichao, L. Experimental study on the wear properties of 42CrMo steel with different microstructures and T15 laser cladding. *J. Mater. Eng. Perform.* **2022**, *31*, 4232–4241. [CrossRef]
98. Xiao, M.; Jiang, F. Microstructural evolution of Fe-based amorphous alloy coatings via ultrasonic vibration-assisted laser cladding. *Mater. Lett.* **2022**, *322*, 132520. [CrossRef]
99. Huang, L.; Zhou, J.; Xu, J.; Huo, K.; He, W.; Meng, X.K.; Huang, S. Microstructure and wear resistance of electromagnetic field assisted multi-layer laser clad Fe901 coating. *Surf. Coat. Technol.* **2020**, *395*, 125876. [CrossRef]
100. Wang, X.L.; Huang, A.R.; Shang, C.J.; Xie, Z.J. Characterization of the cladding layer by laser cladding of 9Cr18Mo powder on 3Cr14 martensitic stainless steel and the impact of martensite obtained through post heat treatment on hardness. *Mater. Today Commun.* **2022**, *32*, 104057. [CrossRef]
101. Guo, W.; Li, X.; Ding, N.; Liu, G.; He, J.; Tian, L.; Chen, L.; Zaïri, F. Microstructure characteristics and mechanical properties of a laser cladded Fe-based martensitic stainless steel coating. *Surf. Coat. Technol.* **2021**, *408*, 126795. [CrossRef]
102. Gong, F.-b.; Shen, J.; Gao, R.-h.; Zhang, T.; Xie, X.; Li, Y. Influence of heat treatment on microstructure and mechanical properties of FeCrNi coating produced by laser cladding. *Trans. Nonferr. Metal. Soc.* **2016**, *26*, 2117–2125. [CrossRef]
103. Da Sun, S.; Fabijanic, D.; Barr, C.; Liu, Q.; Walker, K.; Matthews, N.; Orchowski, N.; Easton, M.; Brandt, M. In-situ quench and tempering for microstructure control and enhanced mechanical properties of laser cladded AISI 420 stainless steel powder on 300M steel substrates. *Surf. Coat. Technol.* **2018**, *333*, 210–219. [CrossRef]
104. Gao, W.; Zhao, S.; Wang, Y.; Zhang, Z.; Zhou, C.; Lin, X. Refinement of Fe-based alloy doped Ti cladding layer. *Surf. Coat. Technol.* **2015**, *270*, 16–23. [CrossRef]
105. Rahman Rashid, R.A.; Nazari, K.A.; Barr, C.; Palanisamy, S.; Orchowski, N.; Matthews, N.; Dargusch, M.S. Effect of laser reheat post-treatment on the microstructural characteristics of laser-cladded ultra-high strength steel. *Surf. Coat. Technol.* **2019**, *372*, 93–102. [CrossRef]
106. Zhu, L.; Yang, Z.; Xin, B.; Wang, S.; Meng, G.; Ning, J.; Xue, P. Microstructure and mechanical properties of parts formed by ultrasonic vibration-assisted laser cladding of Inconel 718. *Surf. Coat. Technol.* **2021**, *410*, 126964. [CrossRef]
107. Liu, W.; Mi, G.; Li, L.; Chen, X.; Pan, Y.; Zhai, F.; Miao, H. Research progress of effect of auxiliary treatment on microstructure and properties of laser cladding layer. *Mater. Rep.* **2023**, *37*, 200–206.
108. Yao, Z.; Shen, Q.; Ge, H.; Wang, Z.; Dong, G.; Ye, Z.; Li, L.; Yao, J. Influence of ultrasound on the wetting behavior of molten pool in laser cladding. *Surf. Technol.* **2022**, *51*, 20–29.
109. Xiao, M.; Jiang, F.; Guo, C.; Song, H.; Dong, T. Investigation on microstructure and mechanical properties of Fe-based amorphous coatings prepared via laser cladding assisted with ultrasonic vibration. *Opt. Laser Technol.* **2023**, *162*, 109294. [CrossRef]
110. Han, X.; Li, C.; Yang, Y.; Gao, X.; Gao, H. Experimental research on the influence of ultrasonic vibrations on the laser cladding process of a disc laser. *Surf. Coat. Technol.* **2021**, *406*, 126750. [CrossRef]
111. Xu, J.; Zhou, J.; Tan, W.; Huang, S.; Wang, S.; He, W. Ultrasonic vibration on wear property of laser cladding Fe-based coating. *Surf. Eng.* **2018**, *36*, 1–9. [CrossRef]
112. Yao, Z.; Wang, F.; Sun, Z.; Chen, Z.; Liu, R.; Yao, J. Effects of ultrasound on distribution of laser melt injected WC reinforced particles on stainless steel substrate surface. *Chin. J. Lasers* **2023**, *50*, 100–109.
113. Wang, Y.; Liu, S.; Zhang, X.; Liu, Y.; Li, R. Experiments and analyses of 3540Fe/CeO_2 coatings by ultrasonic vibration assisted laser cladding. *China Mech. Eng.* **2018**, *29*, 2600–2605.
114. Liu, L.; Feng, M.; Wang, X.; Cui, Y.; Jia, Z.; Li, J. Microstructure analysis of laser cladding strengthening layer on H13 die steel surface assisted by ultrasonic. *Trans. China Weld. Inst.* **2021**, *42*, 85–90+96+102.
115. Wang, Q.; Zhang, L.; Li, Q.; Zhang, J.; Ban, C. Research progress of electromagnetic field assisted laser cladding technology. *Surf. Technol.* **2023**, *52*, 166–179.
116. Lin, Y.; Yuan, Y.; Wang, L.; Hu, Y.; Zhang, Q.; Yao, J. Effect of electric-magnetic compound field on the microstructure and crack in solidified Ni60 alloy. *Acta Metall. Sin.* **2021**, *54*, 1442–1450.
117. Ouyang, W.; Xu, Z.; Chao, Y.; Liu, Y.; Luo, W.; Jiao, J.; Sheng, L.; Zhang, W. Effect of electrostatic field on microstructure and mechanical properties of the 316L stainless steel modified layer fabricated by laser cladding. *Mater. Charact.* **2022**, *191*, 112123. [CrossRef]
118. Li, G.; Wang, Z.; Yao, L.; Xie, D.; Chen, G. Concentration mixing and melt pool solidification behavior during the magnetic field assisted laser cladding of Fe-Cr-based alloy on 45 steel surface. *Surf. Coat. Technol.* **2022**, *445*, 128732. [CrossRef]
119. Chen, Y.; Zhou, J.; Li, P.; Huo, K.; Meng, X.K. Effect of electromagnetic field on wear resistance of Fe901/Al_2O_3 metal matrix composite coating prepared by laser cladding. *Materials* **2022**, *15*, 1531. [CrossRef]
120. Pape, F.; Coors, T.; Barroi, A.; Hermsdorf, J.; Mildebrath, M.; Hassel, T.; Kaierle, S.; Matthias, T.; Chugreev, A.; Chugreeva, A.; et al. Tribological study on tailored-formed axial bearing washers. *Tribol. Online* **2018**, *13*, 320–326. [CrossRef]

121. Chen, C.; Bai, Q.; Zhao, C.; Li, Q.; Zhang, S. Effect of ultrasonic high-frequency micro-forging on the wear resistance of a Fe-base alloy coating deposited by high-speed laser cladding process. *Vacuum* **2024**, *221*, 112934. [CrossRef]
122. Cai, Y.; Shan, M.; Cui, Y.; Manladan, S.M.; Lv, X.; Zhu, L.; Sun, D.; Wang, T.; Han, J. Microstructure and properties of FeCoCrNi high entropy alloy produced by laser melting deposition. *J. Alloys Compd.* **2021**, *887*, 161323. [CrossRef]
123. Zhang, X.; Huang, S.; Li, D.; Geng, J.; Yang, F.; Li, Q. An approach to improve the microstructure and mechanical properties: A hybrid manufacturing of laser directed energy deposition and shot peening. *Addit. Manuf.* **2022**, *55*, 102686. [CrossRef]
124. Zhou, L.; Chen, S.; Jia, W.; Cui, T.; Liang, J. Effects of preheating-ultrasonic synergistic on the microstructure and strength-ductility of 24CrNiMoY alloy steel by laser directed energy deposition. *Mater. Sci. Eng. A* **2023**, *863*, 144463. [CrossRef]
125. Zheng, K.; Lin, Y.; Cai, J.; Lei, C. Corrosion resistance and tribological properties of laser cladding layer of H13 die steel strengthened by ultrasonic rolling. *Chin. J. Mech. Eng.* **2022**, *32*, 137. [CrossRef]